Journal of Science and Transport Technology
Journal homepage: https://jstt.vn/index.php/en

Comparative assessment of EN 1994-1-1, AISC 360 and JGJ 138 for multi-profile composite mega-columns, with a parametric extrapolation towards ultra-high-performance concrete

Hang Mai-Thi*, Thi Thu Tra Nguyen
Faculty of Civil Engineering, Vietnam Aviation Academy, 104 Nguyen Van Troi, Ho Chi Minh City, Vietnam

Article info
Type of article:
Original research paper

DOI:
https://doi.org/10.58845/jstt.utt.2026.en.6.5.234-259

***Corresponding author:**
Email address:
hangmt@vaa.edu.vn

Received: 20/06/2026
Received in Revised Form: 27/09/2026
Accepted: 15/10/2026

Abstract: Mega-columns that embed several discrete hot-rolled profiles in a single reinforced-concrete section, sometimes called isolated steel reinforced concrete (ISRC), have increasingly been adopted in place of welded steel caissons in super-tall lower storeys, but their design falls in a regulatory gap. The simplified method of EN 1994-1-1 covers only single-profile sections, AISC 360-22 admits multiple encased shapes provided they are interconnected but caps the cylinder strength at 69 MPa, and JGJ 138-2016 is confined to concrete grades up to about C80. This study examines how far those provisions can be extrapolated, using a closed-form code-based assessment of a nine-specimen database that combines the six monotonic Phase-1 columns of Bogdan et al. with three axial multi-profile columns of Zhao et al. A single plastic-stress-distribution engine builds the four-point interaction polygon identically under each code, so the only difference is the concrete treatment. All predictions are computed at the characteristic (measured) material level, with partial safety factors set to unity, so that the comparison isolates the cross-sectional mechanics and does not represent factored design capacities. EN 1994-1-1 and AISC 360-22 both apply the 0.85 effective-stress block and coincide, at a mean test-to-prediction ratio λ = 1.12 (CoV 13.4%) against 1.02 for JGJ 138-2016 (CoV 12.2%), whose near-unity α_1 makes it least conservative. The predictions are generally conservative across the eccentric range and for the Zhao cage, the single exception being E10-2 under JGJ 138-2016 (λ = 0.977), but they overpredict Bogdan's two pure-axial specimens at $f'_c \approx$ 55-61 MPa by 11–14% (EN/AISC) and 19–23% (JGJ), reflecting the non-attainment of the full plastic state at peak–the steel still at or below yield and the cover spalling prematurely under full-area loading. In the parametric sweep at e/h = 12.5%, the JGJ margin over the coincident EN/AISC prediction holds within 7–10% up to 180 MPa. Extending these rules to UHPC will require a calibrated effective concrete stress, a minimum steel-fibre dosage, and explicit treatment of eccentricities up to e/h ≈ 15%.

Keywords: Mega-columns, multiple encased steel sections, Eurocode 4, AISC 360, JGJ 138, plastic stress distribution method.

1. Introduction

Steel–concrete composite columns combine the stiffness and ductility of structural steel with the compressive strength and fire endurance of concrete, and have served in tall buildings for several decades. In the lower storeys of super-tall buildings, where gravity and seismic actions are largest, the required cross-sections become unusually large; to carry these actions efficiently while limiting the floor area lost to vertical structure, two solutions have prevailed—concrete-filled welded steel caissons assembled from heavy plates, and reinforced-concrete cross-sections that distribute several discrete hot-rolled profiles across the section. The latter, referred to interchangeably as a multi-steel reinforced concrete (MSRC) column or an isolated steel reinforced concrete (ISRC) mega-column, avoids the heavy welding, preheating, and field repair of welded caissons and exploits readily available rolled sections of large depth.

Bogdan et al. [1, 2] reported a two-phase campaign on ten scaled ISRC mega-columns: six 1/4-scale specimens tested under monotonic axial or eccentric compression, and four 1/6-scale specimens tested under combined axial load and quasi-static cyclic lateral load. Together with the companion analysis of Plumier et al. [3], the campaign showed that full composite action develops even when the four embedded H-sections are not interconnected, that the plane-section assumption remains acceptable for eccentricity ratios up to about 15%, and that the measured capacities are reproduced by an extension of the plastic-stress-distribution principle of EN 1994-1-1 [4].

Several provisions nonetheless complicate routine design. The simplified method of EN 1994-1-1 is restricted by Clause 6.7.3.1(1) to doubly symmetric, uniform cross-sections and is declared not applicable if the structural steel component consists of two or more unconnected sections, which is precisely the configuration considered here; extending its superposition principle to several discrete profiles is mechanically consistent, as Bogdan et al. [1, 2] and Zhao et al. [5] have shown, but it lies outside the declared scope of the standard. ANSI/AISC 360-22 [6] admits cross-sections built up from two or more encased shapes but requires them to be interconnected by lacing, tie plates, or comparable components (Section I2.1e(b) of [6]), and sets out the four-point interaction construction only in Commentary I5 rather than in the body of the Specification, and the effective-stiffness constants of the standard were calibrated on single-profile cross-sections. JGJ 138-2016 [7] restricts its provisions to concrete grades up to about C80, and the work of Lai et al. [8] and Wang et al. [9] indicates that direct application to high-strength concrete encased columns produces noticeable bias relative to test data.

A second consideration concerns the concrete itself. Ultra-high-performance concrete (UHPC), with cylinder strengths of 120–180 MPa and an enhanced post-cracking tensile response provided by steel fibres [10, 11], improves the capacity, ductility and durability of composite columns of many forms [12–15]. Recent tests on encased composite stub columns containing C130-class concrete and S690 steel [16] show that, without steel fibres, the simplified provisions of EN 1994-1-1 and JGJ 138-2016 overestimate the axial capacity of high-strength encased columns, whereas the addition of fibres and closely spaced stirrups restores their predictive accuracy. No published study, to the authors' knowledge, has yet treated a mega-column that combines several embedded hot-rolled profiles with a UHPC matrix; a recent machine-learning study of engineered-cementitious-composite encased steel columns [17] similarly highlights the absence of validated design models for cross-sections that pair multiple encased profiles with high-performance cementitious matrices.

Three gaps therefore remain. First, the

accuracy with which each standard reproduces the published capacities of a multi-profile mega-column, when its simplified principle is extended by superposition, has not been quantified, and no comparison applies the three codes on a strictly common computational basis. Second, the way in which the spread between code predictions evolves as the cylinder strength rises towards the UHPC range - and what that evolution implies for any future code extension - has not been mapped. Third, the influence of cross-sectional architecture, namely discrete encased profiles versus a battened steel cage, on predictive accuracy has not been isolated. This study addresses these gaps through an applied, closed-form assessment that (1) applies a single plastic-stress-distribution engine identically under EN 1994-1-1, AISC 360-22 and JGJ 138-2016 to the nine-specimen database, so that the inter-code differences reduce to the code-specific concrete treatments alone; (2) quantifies, through a parametric extension of the cylinder strength from 30 to 180 MPa, how the inter-code dispersion grows with concrete strength; and (3) reads the contrast between the Bogdan and Zhao specimens as a contrast between two architectural sub-classes of multi-profile mega-column. The study neither proposes a new constitutive model nor adds finite-element simulation.

2. Reference experimental database

Table 1. Geometry and section properties of the nine-specimen database.

Specimen	Steel profiles (n × size, mm)	A_a (mm^2)	ρ_a (%)	d_{sx}, d_{sy} (mm)	A_s (mm^2)	L (mm); L/h
E00-1 – E15-2 (Bogdan)	4 × HEM100 (120×106×12×20)	20,800	10.3	137.5, 137.5	1,608.5	2,700; 6.0
A1, A3 (Zhao)	4 × H120×100×12×12	14,208	7.0	113, 103	1,608.5	1,500; 3.3
A2 (Zhao)	4 × H120×120×8×8	11,008	5.4	103, 103	1,608.5	1,500; 3.3

All cross-sections are 450 × 450 mm. The six Bogdan Phase-1 specimens (E00-1, E00-2, E10-1, E10-2, E15-1, E15-2) share identical geometry and differ only in material strength (Table 2). The longitudinal-reinforcement ratio $\rho_s = A_s / A_g \approx 0.79\%$ throughout; the clear cover to the ties is 10 mm for the Bogdan specimens and 28 mm to the bar centre for the Zhao specimens. dsx and dsy are the profile-centroid offsets from the section centre. L is the physical column length; the unsupported length between the end hinges is 3,590 mm for the Bogdan specimens, giving $l_0/h = 8.0$ [18].

2.1. Specimen geometry and test programme

The reference database comprises two independent programmes on multi-profile encased composite columns: the campaign of Bogdan et al. [1,2] and Plumier et al. [3], complemented by the three axially loaded specimens of Zhao et al. [5]. The Bogdan campaign was conducted in two phases. Phase 1 comprised six 1/4-scale specimens of square 450 mm × 450 mm cross-section and length 2,700 mm, tested under monotonic axial or eccentric compression with the load applied through knife-edge bearings that fixed the nominal eccentricity at the column ends - two specimens at nominal eccentricity ratio e/h = 0 (E00-1, E00-2), two at e/h = 10% (E10-1, E10-2) and two at e/h = 15% (E15-1, E15-2). Owing to second-order deflection of the 2,700 mm columns, the actual eccentricity ratios at peak load exceed the nominal values by 2.4 to 4.9 percentage points, or by 19 to 33% in relative terms, and it is these measured values, reported in Table 2, that are used in the predictions. Phase 2 comprised four 1/6-scale 300 mm × 300 mm specimens tested under combined constant axial load and quasi-static cyclic lateral load; these are revisited only briefly in Section 7 because the monotonic polygonal interaction approach used here is not directly applicable to cyclic capacity. The companion

campaign of Zhao et al. [5] provides three further 450 mm × 450 mm specimens (A1, A2, A3) of length 1,500 mm, each containing four H-section profiles at the corners and tested under pure axial compression with both ends restrained against lateral and rotational movement and only the loaded end free to translate vertically, the critical section being taken at mid-height clear of the end-restraint disturbance. Specimen A4 of the same source is excluded from the present database because it lacked battens and failed in global buckling, outside the validation scope of the simplified method.

An architectural distinction separates the two campaigns and is central to the comparison of Section 5. In the Bogdan Phase-1 specimens, the four HEM100 profiles are placed as discrete encased sections without inter-profile connection, so that composite action develops through bond and bearing on the surrounding concrete only [1, 3]. In the Zhao specimens, the four corner H-sections are tied by horizontal battens (50 × 6 to 50 × 12 mm at 200 mm pitch) into a closed steel cage around an inner concrete core [5]; this cage partitions the cross-section into regions of qualitatively different confinement state, including a highly steel-confined inner core (HSCC, in the terminology of Zhao et al. [5]) that has no analogue in the discrete-profile Bogdan configuration.

The Phase-1 cross-section contained four hot-rolled HEM100 profiles of nominal dimensions 120 × 106 × 12 × 20 mm arranged in a cruciform pattern, one at the middle of each side (Fig. 1(a)), centred at a distance d_p = 137.5 mm from the section centre and confined by transverse ties of 3.25 mm diameter at 80 mm pitch; the longitudinal reinforcement was distributed around the perimeter to a total area A_s = 1,608.5 mm^2 (reinforcement ratio $\rho_s \approx 0.79\%$, computed directly from Tables 3-3 and 3-4 of [18]), with a clear cover to the ties of 10 mm. The total area of the four profiles was about 20,800 mm^2, giving a structural-steel ratio of approximately 10.3%–comfortably within the 4-15% range required by JGJ 138-2016 [7]. The Zhao specimens A1 and A3 each contained four H120×100×12×12 profiles (A_a = 14,208 mm^2, $\rho_a \approx$ 7.0%), while A2 contained four H120×120×8×8 profiles (A_a = 11,008 mm2, $\rho_a \approx$ 5.4%, computed from the gross section; Zhao et al. [5] report 4.8% for this specimen); all three used A_s = 1,608.5 mm^2 ($\rho_s \approx 0.79\%$) and ties with a diameter of 10 mm diameter, with a cover of 28 mm measured to the bar centre, giving an effective lever arm d_s = H/2 − 28 = 197 mm. Because A1–A3 were tested in pure axial compression, this lever arm enters only the flexural vertices of their interaction polygon and not the axial capacity that governs their λ. The cross-section and loading arrangement of the Phase-1 specimens are shown in Fig. 1, and those of the Zhao axial specimens in Fig. 2. The geometry and section properties of the nine specimens are collected in Table 1.

This study validates the cross-sectional N–M resistance predicted by the plastic-stress-distribution provisions, not the complete member-design procedures of the three standards. Because the measured eccentricities at peak load already contain the second-order deflection of the test columns, the P–δ amplification is carried on the demand side, and the member-stability provisions are not invoked: the buckling-curve reduction χ of EN 1994-1-1, the P_{no}–P_e interaction with effective stiffness $(EI)_{eff}$ of AISC 360-22, and the stability coefficient ϕ with moment magnification of JGJ 138-2016. Entering the nominal eccentricities with each code's second-order provisions instead would reintroduce code-specific member-level assumptions, namely the effective flexural stiffness, the imperfections, and the additional eccentricity, whose calibration for multi-profile sections is itself unverified. The measured amplification of the eccentricity, 19 to 33% at peak load, indicates the order of the second-order effect that such provisions would have to reproduce; this member-level comparison is identified as future work in Section 7.4.

Table 2. Measured material strengths of the Phase-1 specimens (Table 3-2 of [18]) and the equivalent values used in the predictions (the three Zhao specimens [5] are listed for completeness).

Specimen	e/h actual (%)	f_{cu} (MPa)	f_{ck} (MPa)	f_{yf} flange (MPa)	f_{yw} web (MPa)	$f_{y,eq}$ used (MPa)
E00-1	0.0	61.2	61.2	408	523	429
E00-2	0.0	56.6	55.0	398	411	400
E10-1	12.4	60.9	56.4	423	435	425
E10-2	12.9	72.8	59.2	383	415	389
E15-1	19.9	66.1	57.2	377	404	382
E15-2	17.9	67.6	56.3	389	405	392
A1	0.0	—	45.0	300	300	300
A2	0.0	—	49.5	283	283	283
A3	0.0	—	44.8	261	261	261

f_{cu} is the measured cube strength; f_{ck} is the directly measured concrete axial strength reported in CTBUH Table 3-2 [18] (specimen geometry not stated in the source; see Section 7.4). For the Bogdan specimens, the longitudinal-rebar yield strength is 438 MPa, and the measured tie yield strength is 597 MPa (Table 3-2 of [18]; the value annotated in Fig. 1(a) is the specified grade HRB 500, f_{yk} = 500 MPa); for the Zhao specimens f'_c is reported directly in cylinder form, the longitudinal-rebar yield strength is 521 MPa, and the tie yield strength is 571 MPa [5].

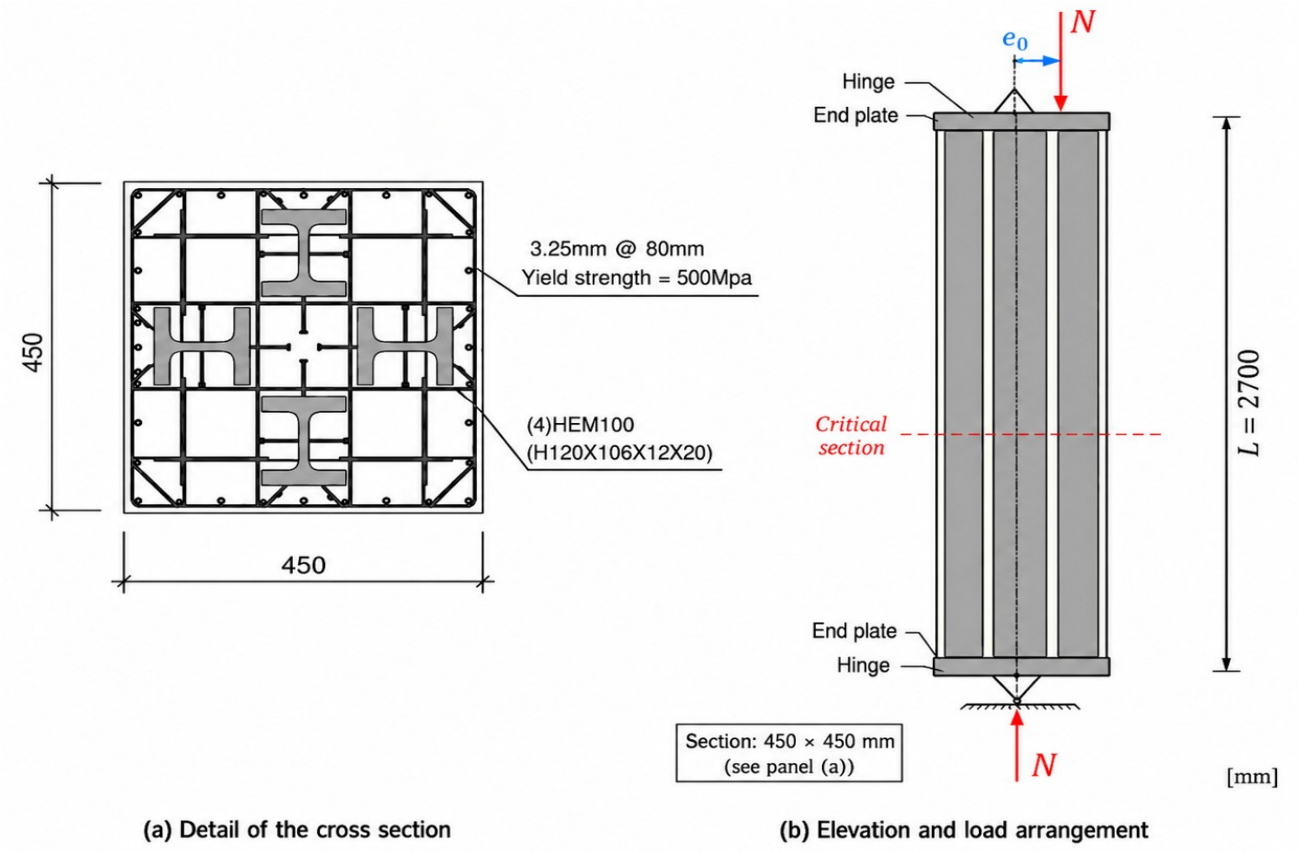


Fig. 1. Phase 1 reference specimen: (a) cross-section with four HEM100 profiles and longitudinal /transverse reinforcement; (b) elevation showing supports and load application. (adapted from [1, 2, 18]). The tie strength in (a) is the specified grade HRB 500; the measured value is 597 MPa (Table 2).

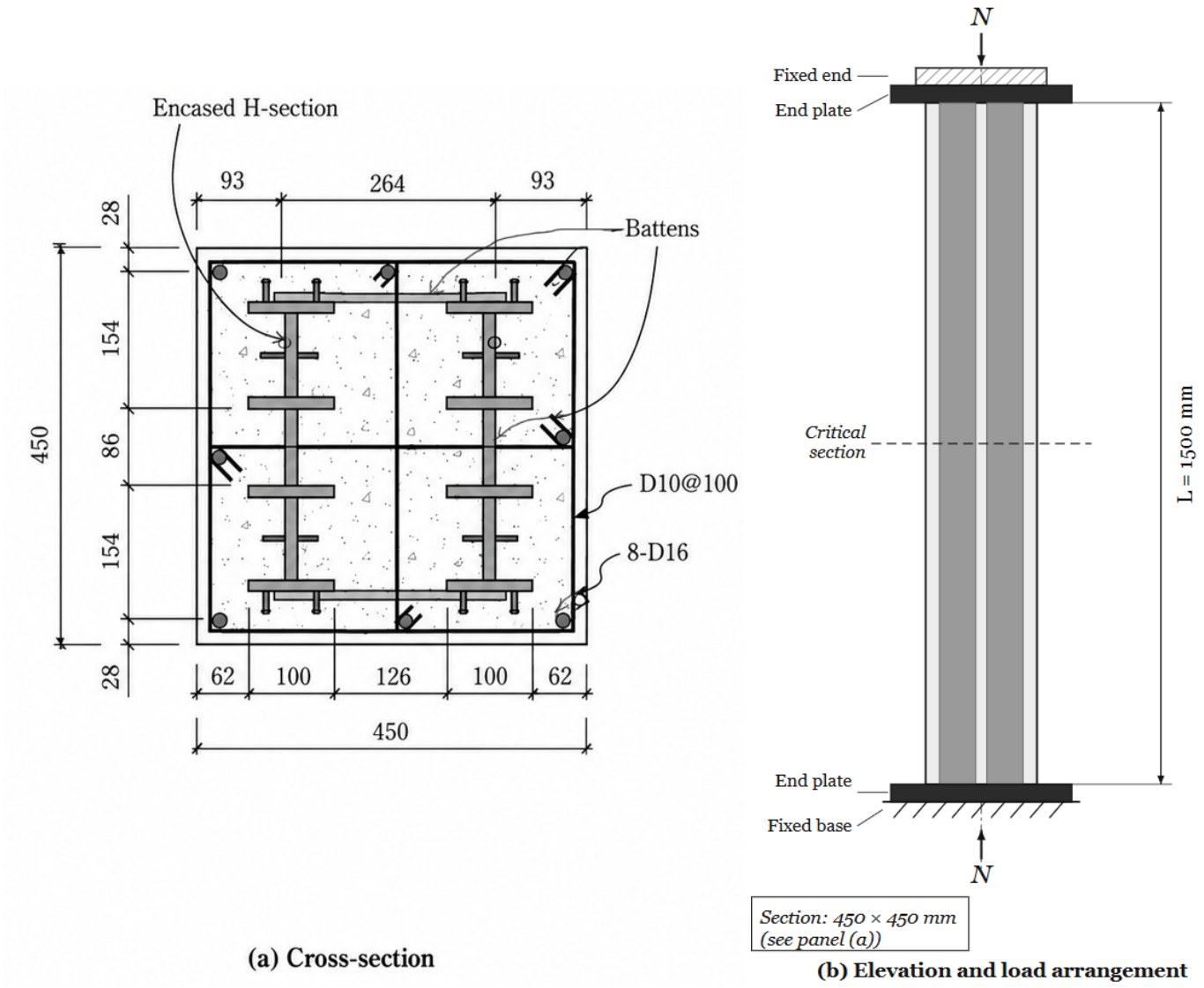


Fig. 2. Specimens and test setup for axial load tests of Zhao et al. [5].

2.2. Material properties

The measured material strengths reported in Table 3-2 of [18] are summarised in Table 2. For each Phase-1 specimen, Table 3-2 of [18] reports two distinct concrete strengths: a cube strength f_{cu} on 150 mm companion cubes and a separately reported concrete axial strength $f_{c,axial}$ from a uniaxial compressive test. In the present comparison, $f_{c,axial}$ is adopted directly as the input cylinder strength f'_c for all three codes, on the grounds that it is the in-situ uniaxial strength most directly comparable to the f'_c on which the code formulas are calibrated and that it removes any need for a cube-to-cylinder conversion. Throughout, f'_c and f_{ck} denote this measured input strength, not a 5%-fractile characteristic value, the partial material factors being set to unity (Section 3.4). The per-specimen ratio $f_{c,axial}/f_{cu}$ ranges from 0.81 to 1.00 with a mean of 0.90 - consistent both with a 150×300 mm cylinder under EN/ACI conventions ($f_{cyl}/f_{cu} \approx 0.80–0.85$ over the classes C45/55 to C60/75) and with a 150×150×300 mm prism under GB/T 50081 [19] ($f_{prism}/f_{cu} \approx 0.85–0.90$) - rather than tracking a single conversion factor; the scatter indicates that the two columns of Table 3-2 of [18] are independent measurements on companion specimens of each concrete batch, a cylinder for $f_{c,axial}$ and a 150 mm cube for f_{cu}, rather than the application of a uniform code conversion, and the robustness of the test-to-prediction ratios to this interpretation is quantified in Section 7.4. The flange and web yield strengths are reported

separately because they originate from different rolling batches, so an equivalent yield strength $f_{y,eq}$ is computed as the area-weighted average of the flange and web values,

Table 3. Provisions of the three standards relevant to the present comparison, and the form in which each is applied in this study. Clause, equation and table numbers refer to EN 1994-1-1:2004 [4], AISC 360-22 [6] and JGJ 138-2016 [7], respectively.

Aspect	EN 1994-1-1:2004	AISC 360-22	JGJ 138-2016
Cross-sectional axial resistance	$N_{pl,Rk} = A_a \cdot f_y + 0.85 \cdot A_c \cdot f_{ck} + A_s \cdot f_{sk}$ (Eq. 6.30, Cl. 6.7.3.2(1)); the 0.85 is replaced by 1.0 for concrete-filled sections	$P_{no} = F_y \cdot A_s + F_{ysr} \cdot A_{sr} + 0.85 \cdot f'_c \cdot A_c$ (Eq. I2-7, Sect. I2.1b of [6])	$N \le 0.9 \cdot \phi \cdot (f_c \cdot A_c + f_{ya} \cdot A_a + f_{ys} \cdot A_s)$, $f_c = \alpha_1 \cdot f_{ck}$, as reproduced in [18]. The factor 0.9 and φ are set to unity in this study (Section 3.3)
Concrete stress-block factor	0.85 (fully and partially encased sections)	0.85	$\alpha_1 = 1.00$ up to C50, decreasing linearly to 0.94 at C80
Concrete strength limit	C20/25–C50/60 for composite columns (Cl. 6.7.1(2)P); the standard as a whole covers to C60/75, and C70/85 is admitted in EN 1994-1-1:2026 [20]	3–10 ksi (21–69 MPa) for normal-weight concrete (Sect. I1.3(a) of [6]); Appendix 2 extends to 15 ksi for filled sections only	≈ C80
Multiple encased profiles	Explicitly excluded: the simplified method is not applicable if the structural steel component consists of two or more unconnected sections (Cl. 6.7.3.1(1) of [4])	Admitted, but Sect. I2.1e(b) of [6] requires two or more encased shapes to be interconnected by lacing, tie plates or comparable components; the four-point interaction construction is given in Commentary I5 (Method 2), not in the Specification body	Permitted, with a structural-steel ratio of 4–15%
Other scope limits	S235–S460 (Cl. 6.7.1(2)P); $0.2 \le \delta \le 0.9$ (Eq. 6.27); $\bar{\lambda} \le 2.0$ (Eq. 6.28); cover usable in calculation max $c_y = 0.4b$, max $c_z = 0.3h$ (Eq. 6.29); longitudinal reinforcement usable in calculation ≤ 6% of the concrete area (Cl. 6.7.3.1(3)) and ≥ 0.3% (Cl. 6.7.5.2(1)); depth-to-width ratio 0.2–5.0 (Cl. 6.7.3.1(4))	Steel core ≥ 1% of the total composite cross-section (Sect. I2.1a(a)); $\rho_{sr} \ge 0.004$ (Eq. I2-1); $F_y \le 75$ ksi (525 MPa); $F_{ysr} \le 80$ ksi (550 MPa) (Sect. I1.3 of [6])	Structural-steel ratio 4–15%
Member stability	χ from EN 1993-1-1, Cl. 6.3.1.2; Table 6.5 of [4] assigns fully encased sections curve b about y-y (α = 0.34) and curve c about z-z (α = 0.49)	$P_n = P_{no} \cdot 0.658^{\wedge}(P_{no}/P_e)$ for $P_{no}/P_e \le 2.25$, otherwise $P_n = 0.877 \cdot P_e$ (Eqs I2-2, I2-3), with $P_e = \pi^2 (EI)_{eff}/L_c^2$ and $(EI)_{eff} = E_s I_s + E_s I_{sr} + C_1 E_c I_c$, $C_1 = 0.25 + 3(As + A_{sr})/A_g \le 0.7$. Commentary I5 applies the same ratio P_n/P_{no} to the axial ordinate of points A, C, D and E	ϕ tabulated against l_0/i, ϕ = 1.00 for $l_0/i \le 28$, where $i = \sqrt{[(E_c I_c + E_a I_a)/(E_c A_c + E_a A_a)]}$

Table 3. (continued)

Aspect	EN 1994-1-1:2004	AISC 360-22	JGJ 138-2016
Member imperfection	Equivalent bow imperfection L/200 about y-y and L/150 about z-z (Table 6.5 of [4])	Direct analysis with notional loads $N_i = 0.002\alpha Y_i$ (Eq. C2-1) or explicit modelling of the initial out-of-plumbness; $\tau_b = 0.8$ for composite members (Sect. I1.5(d))	$e_a = \max(20\ \text{mm}, h_c/30)$
Second-order amplification	$k = \beta/(1 - N_{Ed}/N_{cr,eff}) \geq 1.0$ with $\beta = 0.66 + 0.44r \geq 0.44$ (Eq. 6.43 and Table 6.4 of [4]), $N_{cr,eff}$ from $(EI)_{eff,II} = 0.9\cdot(E_a I_a + E_s I_s + 0.5\cdot E_{cm} I_c)$ (Eq. 6.42)	$B_1 = C_m/(1 - \alpha P_r/P_{e1}) \geq 1$, $C_m = 0.6 - 0.4(M_1/M_2)$ (Eqs A-8-3, A-8-4)	$M = \eta\cdot N\cdot ei$ with $e_i = e_0 + e_a$ and $\eta = 1 + (l_0/h)^2\cdot\zeta_1\cdot\zeta_2/(1400\cdot e0/h_0)$
Safety format (not applied here)	Material partial factors γ_c, γ_s, γ_a; the member check also carries $\alpha_M = 0.9$ for S235–S355 and 0.8 for S420–S460 (Cl. 6.7.3.6(1))	Resistance factors $\phi_c = 0.75$ in compression and $\phi_b = 0.90$ in flexure (LRFD)	The 0.9 factor above, material design strengths, and the seismic factor γ_{RE}
As applied in the present study	Measured strengths; $\gamma = 1$; cross-section resistance only; the second-order effect is carried on the demand side through the measured eccentricities	Same	Same; α_1 keyed to the measured cube grade; $\phi = 1.0$ ($l_0/i = 26.5 \leq 28$) and the 0.9 factor set to unity

$$f_{y,eq} = \frac{A_{fl} f_{yf} + A_{web} f_{yw}}{A_{fl} + A_{web}} \quad (1)$$

where $A_{fl} = 2\cdot b_p\cdot t_f$ and $A_{web} = t_w\cdot(h_p - 2\cdot t_f)$ are the flange and web areas of the rolled profile; this gives $f_{y,eq}$ = 382-429 MPa across the six Phase-1 specimens (Table 2). The Zhao specimens [5] report f'_c directly as a cylinder strength, a convention confirmed by their use of the modulus expression $E_c = 5{,}000\cdot(f'_c)^{1/2}$, so no conversion is applied; the four profiles of each Zhao specimen were rolled from a single batch and share one yield strength, so the area-weighted averaging used for the Bogdan flange/web mismatch is unnecessary.

The ratio $f_{c,axial}/f_{cu}$ is highest for the two pure-axial specimens, 1.000 for E00-1 and 0.972 for E00-2, against 0.813–0.926 for the four eccentric specimens, and the two columns of the source table disperse differently, the axial strengths spanning 55.0–61.2 MPa (CoV 3.9%) against 56.6–72.8 MPa (CoV 9.0%) for the cubes. Bogdan et al. [1] attribute the shortfall of E00-1 and E00-2 to concrete strengths below the six-specimen average, a diagnosis that holds in cube terms but is reversed under the $f_{c,axial}$ convention, which makes E00-1 the strongest of the six. Section 7.4 quantifies the consequence: under the cube-based route $f'_c = 0.80\cdot f_{cu}$, λ rises from 0.899 to 0.997 for E00-1 and from 0.878 to 0.960 for E00-2 under EN 1994-1-1 = AISC 360-22 (from 0.837 to 0.936 and from 0.815 to 0.897 under JGJ 138-2016), which places the greater part of the pure-axial bias of Section 5.2 in the $f_{c,axial}$ column of the source table rather than in the specimens. That route is not adopted, because it makes the eccentric predictions considerably more conservative (Section 7.4), and the $f_{c,axial}$ basis is retained as the directly measured value requiring no conversion.

2.3. Test results adopted as benchmark

The peak axial loads at failure are taken from Bogdan et al. [1] for the six Phase-1 specimens and from Zhao et al. [5] for A1–A3, and are reproduced in Table 4. The peak loads span 12,041 kN (E15-1, e/h ≈ 20%) to 17,082 kN (E00-1, e/h = 0) for Bogdan and lie tightly between 15,058 kN and

15,143 kN for the three Zhao specimens. The bending moment at the mid-height critical section is $M_{test} = N_{test} \times e$, where e is the actual eccentricity at failure. These (N_{test}, M_{test}) pairs form the empirical reference points against which the predictions are compared in Section 5. The five pure-axial specimens (E00-1, E00-2 and A1–A3) therefore enter the comparison as (N_{test}, 0) points at the apex of the interaction polygon, while the four eccentric Bogdan specimens enter as (N_{test}, M_{test}) points on its upper branch.

3. Code provisions for encased composite columns

This section identifies, for each standard, the specific assumptions adopted in the present comparative calculation rather than reproducing the codes in full (see Table 3)

3.1. EN 1994-1-1: simplified method

Table 4. Measured peak forces and code predictions at the actual eccentricity (nine specimens: six Bogdan [1], three Zhao [5]). EN 1994-1-1 = AISC 360-22 (both apply the 0.85 block); $M_{pred} = N_{pred} \cdot e$, non-zero only for the four eccentric specimens.

Specimen	e (mm)	N_{test} (kN)	M_{test} (kN·m)	N_{EC4} = AISC (kN)	N_{JGJ} (kN)	M_{EC4} = AISC (kN·m)	M_{JGJ} (kN·m)
E00-1	0.0	17,082	0	19,001	20,407	0	0
E00-2	0.0	15,325	0	17,452	18,807	0	0
E10-1	55.8	14,360	801	12,824	13,929	716	777
E10-2	58.0	13,231	767	12,622	13,544	732	786
E15-1	89.6	12,041	1,079	10,589	11,500	949	1,030
E15-2	80.6	12,759	1,028	11,009	11,916	887	960
A1	0.0	15,143	0	12,241	13,501	0	0
A2	0.0	15,058	0	11,943	13,353	0	0
A3	0.0	15,089	0	11,655	12,910	0	0

Clause 6.7.3 of EN 1994-1-1 [4] provides a simplified method for composite columns of doubly symmetric and uniform cross-section. The plastic resistance to compression is the sum of the component plastic resistances,

$$N_{pl,Rk} = A_a f_y + 0.85 A_c f_{ck} + A_s f_{sk} \quad (2)$$

where A_a, A_c and A_s are the areas of the structural steel, the concrete and the longitudinal reinforcement, and f_y, f_{ck} and f_{sk} are the corresponding characteristic strengths. For fully encased members Clause 6.7.3.2(1) carries the 0.85 multiplier on f_{ck} shown in Eq. (2) - the reduction from the cylinder strength to the in-situ design stress of a concentrically loaded prism - and substitutes unity for it only in concrete-filled tubes, where the steel casing supplies the missing confinement; the encased mega-column therefore retains the 0.85 block, which is the same factor prescribed by AISC 360-22, so that the two standards predict an identical axial vertex (Section 5.2). The axial-flexural interaction is approximated by a polygon through points A (pure compression, $N_A = N_{pl,Rk}$, M = 0), B (pure bending, N = 0, $M = M_{pl,Rk}$), C (the same plastic moment as B but at the concrete-only axial force $N_{pm,Rk} = 0.85 \cdot A_c \cdot f_{ck}$) and D (one half of $N_{pm,Rk}$ at a moment slightly larger than $M_{pl,Rk}$). Clause 6.7.3.1(1) declares the method not applicable if the structural steel component consists of two or more unconnected sections, and Clause 6.7.3.1(3) limits the longitudinal reinforcement that may be used in calculation to 6% of the concrete area, against 0.79% here.

3.2. ANSI/AISC 360-22: plastic-stress-distribution method

Section I2.1 of AISC 360-22 [6] gives the

nominal axial compressive strength of an encased member as

$$P_{no} = F_y A_s + F_{ysr} A_{sr} + 0.85 f'_c A_c , \quad (3)$$

where A_s and A_{sr} denote the structural-steel and longitudinal-reinforcement areas (A_a and A_s in the present notation). AISC applies the same 0.85 factor to the concrete strength as EN 1994-1-1 (Eq. (2)), so that the two standards return identical axial capacities for the present sections; the substantive divergence lies elsewhere. AISC accommodates more than one encased steel shape only obliquely: the case is recognised in the detailing requirements of Section I2.1e(b) of [6], which requires a cross-section built up from two or more encased shapes to be interconnected by lacing or tie plates against buckling of the individual shapes before the concrete hardens, while the limitation that the steel core comprise at least 1% of the composite section is given separately in Section I2.1a of [6]. The nominal strength of the composite section is to be obtained by the plastic-stress-distribution method of Section I1.2a of [6] - steel at F_y, concrete at $0.85 \cdot f'_c$ - yet the construction of the axial–flexural interaction diagram is not set out in the body of the Specification: Section I5 defers it to the interaction equations of Section H1.1 of [6] or to the methods of Section I1.2 of [6], and the only explicit multi-point construction appears in the Commentary, framed for a single encased profile, so that its application to a multi-profile section rests on the same superposition principle as EN 1994-1-1. AISC 360-22 also caps the specified concrete strength at 10 ksi (69 MPa) for normal-weight members and the structural-steel yield stress at 75 ksi (525 MPa) [6, Section I1.3], so the application of Eq. (3) to UHPC lies strictly outside its scope.

3.3. JGJ 138-2016: Chinese composite structures code

JGJ 138-2016 [7] gives rules for composite columns with one or more encased profiles, subject to a structural-steel ratio of 4–15% and a concrete grade typically up to C80. The nominal axial capacity follows.

$$N_u = \phi (f_c A_c + f_y A_a + f_{ys} A_s) \quad (4)$$

where the effective concrete stress is $f_c = \alpha_1 \cdot f_{ck}$, the JGJ counterpart of the $0.85 \cdot f_{ck}$ block of Eqs. (2) and (3); the longitudinal reinforcement is taken at the same characteristic strength f_{sk} as in Eq. (2) (written f_{ys} in the present form of Eq. (4)); φ is a stability coefficient that decreases from 1.0 for stocky columns ($L/h \le 8$) to lower values for slender ones. The code writes this axial resistance with a factor of 0.9 ahead of the stability coefficient, $N \le 0.9 \cdot \phi \cdot (f_c \cdot A_c + f_{ya} \cdot A_a + f_{ys} \cdot A_s)$, as reproduced in [18]. That factor is set to unity here, for three reasons. It is a reliability allowance for accidental eccentricity rather than a term of the cross-sectional mechanics, so retaining it while the partial factors of the other two standards are set to unity would bias the comparison against JGJ 138-2016. In the design framework set out in [18], it belongs to the member-level step, alongside the buckling and second-order provisions, and not to the step that establishes the nominal cross-sectional capacity, so it falls outside the scope defined in Section 2.1; the same source applies only ϕ when tabulating nominal capacities and introduces the material factors separately. And it attaches to the pure-axial branch alone, the eccentric-compression provisions carrying no counterpart, so applying it at vertex A while points B, C and D remain unreduced would leave the interaction polygon discontinuous. The consequence of retaining it is quantified in Section 7.2. For the Bogdan specimens the unsupported (buckling) length between the end hinges is l_0 = 3,590 mm (CTBUH Table 3-4 [18]), measured to the centres of the two knife-edge end hinges and therefore exceeding the 2,700 mm physical column length, giving l_0/h = 8.0; with $i = \sqrt{[(E_c I_c + E_a I_a)/(E_c A_c + E_a A_a)]}$ as defined by the code, l_0/i = 26.5, within the $l_0/i \le 28$ range of the stability table (the value kl_u/r = 27.6 reported in Table 3-4 of [18] is the ACI 318 slenderness), at the upper edge of the stocky range; because the measured second-order eccentricities of Table 2 are used directly, the P–δ amplification is carried in the

demand rather than through φ, and φ = 1.0 is adopted. Following the tradition of GB 50010-2010 [21], a reduction factor α_1 is applied to the rectangular concrete stress block once the concrete grade exceeds C50, decreasing linearly from 1.00 at grade C50 to 0.94 at grade C80, with a floor of 0.94, to reflect the more brittle response of high-strength concrete. Consistent with the GB 50010 definition, α_1 is keyed to the cube-strength grade f_{cu}, and the resulting effective stress $\alpha_1 \cdot f_{ck}$ is carried through every vertex of the interaction polygon, including the pure-axial capacity; for the present specimens the cube grades stay at or below C80, so α_1 lies between 0.94 and 1.00, while in the parametric study of Section 6 the same rule is keyed to the swept cylinder strength. Because α_1 is confined to the interval [0.94, 1.00], the keying variable - the cube grade for the tested specimens and the cylinder strength as a proxy for the Zhao specimens and throughout the parametric sweep - shifts the effective concrete stress by at most 6%, and at $f_{ck} \geq 80$ MPa α_1 reaches its 0.94 floor under either convention, so the inter-code comparison and its trend towards the UHPC range (Section 6) are insensitive to the keying, even though the precise strength at which α_1 leaves unity is not. Carrying α_1 to the pure-axial vertex departs from a strict reading of GB 50010, in which α_1 is the equivalent-rectangular-block factor for flexure and the squash load uses the unreduced axial strength; the uniform treatment is adopted so that the three codes differ only in the scalar concrete multiplier at every vertex, and it is conservative for JGJ - restricting α_1 to the flexural vertices would raise the JGJ axial capacity and deepen the pure-axial non-conservatism reported in Section 5.2, not relieve it.

3.4. Synthesis

This study compares the resistance provisions of the three standards as implemented within a unified cross-sectional plastic-stress-distribution framework at the characteristic material level. It does not compare the complete design procedures, which differ further in stability treatment, second-order provisions and safety format (see Table 3).

The three standards share the same mechanics-superposition of the plastic resistances of steel, concrete and reinforcement - but differ in three respects relevant here: the multiplier on the concrete cylinder strength in the axial-capacity equation (0.85 in EN 1994-1-1 and AISC 360-22 alike, since both invoke the encased-section block, against $\alpha_1 \cdot f_{ck}$ in JGJ 138-2016, with α_1 staying at unity up to C50 and falling only to 0.94 at C80); the explicit treatment of multi-profile sections (excluded by EN 1994-1-1, admitted conditionally by AISC 360-22 and permitted by JGJ 138-2016; none specifies the multi-profile interaction construction; see Table 3); and the upper limit on concrete strength (C50/60 in the simplified method of EN 1994-1-1:2004, extended to C70/85 in the second-generation EN 1994-1-1:2026 [20]; 69 MPa in AISC 360-22; ≈ C80 in JGJ 138-2016). None of the three admits UHPC strength classes above 120 MPa within its simplified method, so the high-strength predictions of Section 6 are extrapolations of identical mechanics under three different concrete treatments. All three sets of predictions in this study are computed at the characteristic material level, with partial factors set to unity, so that the comparison isolates the mechanics; the agreement between codes does not carry over to design-level capacities, since EN 1994-1-1 applies the material partial factors γ_c, γ_s and γ_a whereas JGJ 138-2016 divides the material strengths by γ_{RE} together with a global resistance factor.

4. Methodology of the predictions

4.1. Geometric idealisation

The cross-section is treated as a homogeneous 450 × 450 mm rectangle containing four profiles centred at a distance d_p = 137.5 mm from the section centre for the Bogdan specimens; for the Zhao specimens A1 and A3 the corner profiles lie at d_{sx} = 113 mm and d_{sy} = 103 mm, read

from the dimensioning chain of Zhao et al. [5, Fig. 2], and for A2 a common 62 mm outer cover yields $d_{sx} = d_{sy} = 103$ mm. The longitudinal reinforcement is idealised as a lumped layer at an effective lever arm $d_s \approx H/2 - \text{cover} - d_{tie} - d_{bar}/2$ from the centroid, and the concrete area equals the gross area less the steel and reinforcement areas. For the Bogdan specimens, this lever arm is $d_s = 225 - 10 - 3.25 - 4 = 207.75$ mm, and the four rolled profiles are represented by their actual areas at their actual centroid offsets d_p rather than by a single equivalent profile at the section centre, so that the superposition of plastic resistances captures the distributed multi-profile geometry directly. The bending axis is the strong axis of the composite section; for the doubly symmetric Bogdan cruciform the strong- and weak-axis surfaces coincide, while for the Zhao specimens A1 and A3 the two principal-axis surfaces differ by a few per cent, a difference immaterial to the comparison because A1–A3 were loaded in pure axial compression (e = 0), for which only N_{pl} is required and the bending axis is irrelevant. In the ultimate state, all steel components are assumed to yield in tension or compression, and the concrete in compression carries a uniform stress equal to the code-specific block ($0.85 \cdot f_{ck}$ for EN 1994-1-1 and AISC 360-22, $\alpha_1 \cdot f_{ck}$ for JGJ 138-2016), with the concrete in tension neglected. The equivalent-plate idealisation of the section and the resulting four-point interaction polygon are shown schematically in Fig. 3.

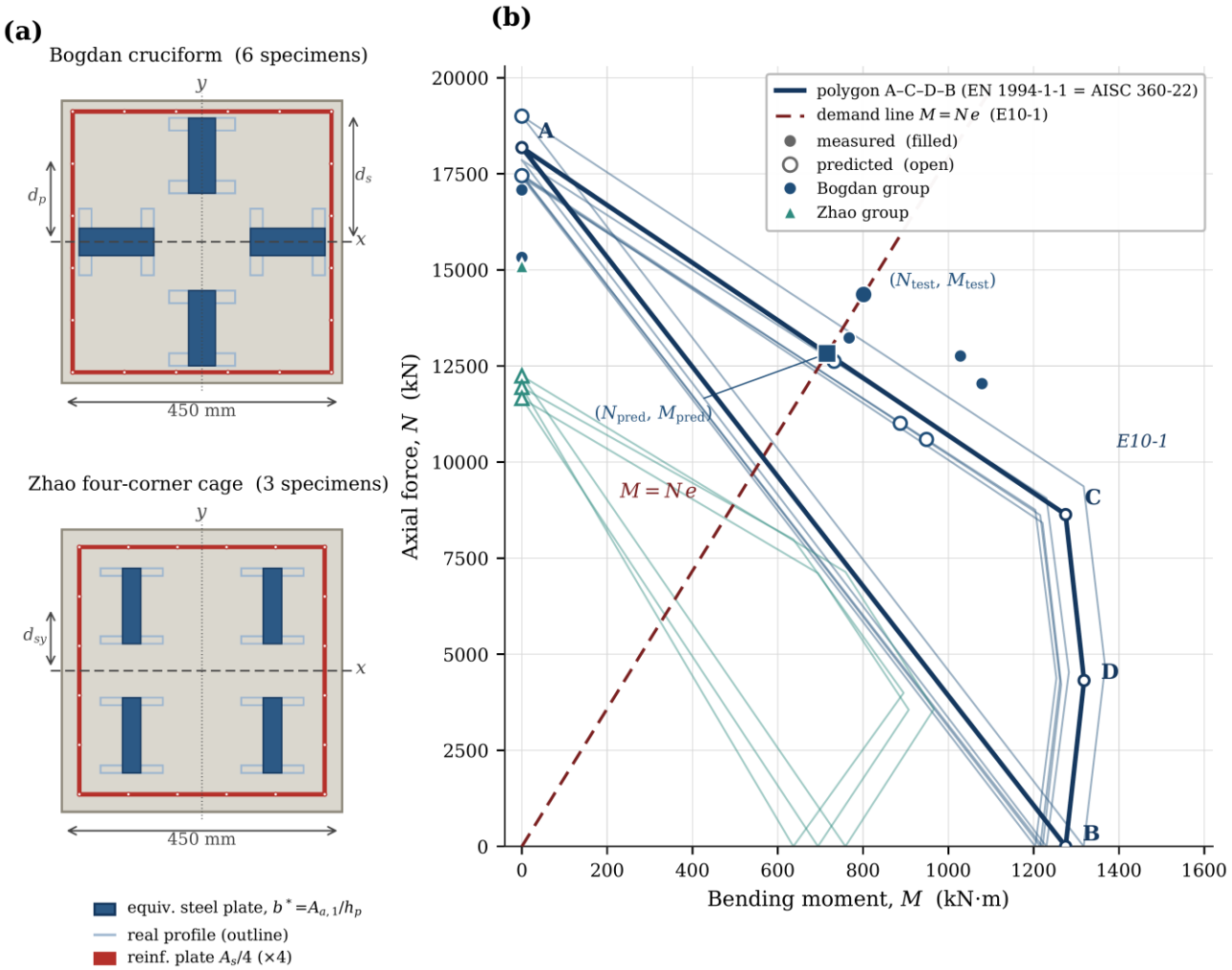


Fig. 3. Prediction method: (a) cross-section idealised as equivalent rectangular plates (reinforcement as four $A_s/4$ plates); (b) four-point interaction polygon A–C–D–B with demand line M = N·e meeting A–C at (N_{pred}, M_{pred}).

4.2. Construction of the polygonal interaction curve

For each code, the polygon is constructed at the four points A, B, C and D following the plastic-stress-distribution method of EN 1994-1-1 §6.7.3.2, extended to multi-profile sections after Bogdan et al. [2] and CTBUH [18]. Point A is the plastic axial capacity $N_{pl,Rd}$ from the corresponding axial-capacity equation (with $\phi = 1.0$ for the stocky specimens). Point D is the maximum bending resistance $M_{max,Rd}$, reached when the plastic neutral axis (PNA) coincides with the axis of symmetry, at axial force $N_{pm,Rd}/2$, where $N_{pm,Rd} = A_c \cdot f_{c,eff}$ is the concrete-only contribution and $f_{c,eff} = 0.85 \cdot f_{ck}$ (EN 1994-1-1 and AISC 360-22) or $\alpha_1 \cdot f_{ck}$ (JGJ 138-2016). The maximum moment is evaluated from the plastic section moduli of the constituents.

$$M_{max,Rd} = W_{y,steel} f_{y,eq} + W_{s,rebar} f_s + 0.5 W_c f_{c,eff} \quad (5)$$

The factor 0.5 on W_c reflects that the rectangular concrete block acts on a single side of the PNA. The plastic modulus of the four profiles is $W_{y,steel} = 2 \cdot A_{a,one} \cdot d_{sy} + 2 \cdot Z_y$ for the Bogdan cruciform and $W_{y,steel} = 4 \cdot A_{a,one} \cdot d_{sy}$ for the Zhao four-corner layout, where $A_{a,one} = A_a/n$ is the area of one profile. In the cruciform the two profiles offset along the bending direction contribute the parallel-axis term $2 \cdot A_{a,one} \cdot d_{sy}$, whereas the two transverse profiles, rotated through 90°, present their minor axis to the bending plane and each contribute their own minor-axis plastic modulus $W_{pl,z} \approx W_{pl,y}/2$ (a section-specific equality: for the HEM100 profiles used here the catalogue minor-axis modulus of about 116 cm³ matches half the strong-axis value, ≈ 118 cm³, and it is not a general property of H-sections), so that the pair contributes $2 \cdot Z_y$ with $Z_y = W_{pl,y}/2$; representing this pair instead by their strong-axis modulus would overstate $W_{y,steel}$ by roughly 14% and is avoided. The longitudinal reinforcement is idealised, following Bogdan et al. [2], as two equivalent horizontal plates of area $A_{s1} = A_s/4$ at $\pm d_s$ plus two equivalent vertical plates of area $A_{s2} = A_s/4$ spanning between them, the four plates conserving the cage area A_s; with $h_{s2} = 2 \cdot d_s$ and $b_{s2} = A_{s2}/h_{s2}$, this gives

$$W_{s,rebar} = 2A_{s1}d_s + \frac{b_{s2}h_{s2}^2}{2} = 0.75A_s d_s, \quad (6)$$

which is bounded above by the discrete-cage value $A_s \cdot d_s$. The concrete modulus follows by complementarity, $W_c = B \cdot H^2/4 - W_{y,steel} - W_{s,rebar}$, with B the width perpendicular to the bending axis and H the depth along it. Points B and C share the plastic moment $M_{pl,Rd}$, obtained by subtracting from $M_{max,Rd}$ the plastic contributions of the central band $[-h_n, +h_n]$ whose stress state reverses between B and D, namely $M_{pl,Rd} = M_{max,Rd} - (W_{yn} \cdot f_{y,eq} + W_{sn} \cdot f_s + 0.5 \cdot W_{cn} \cdot f_{c,eff})$, where W_{yn}, W_{sn} and W_{cn} are the section moduli of the profiles, reinforcement and concrete within that band. The PNA shift h_n follows from axial equilibrium between B and C in closed form. For the cruciform layout three scenarios are distinguished according to whether the neutral axis lies within the inner equivalent plates ($0 \le h_n \le b^*/2$), between the two profile plates ($b^*/2 < h_n \le d_d/2$) or within the outer plates ($d_d/2 < h_n \le (d_d + h_p)/2$), each giving a force-balance expression in which the steel terms reverse sign through the $(2 \cdot f_y - f_{c,eff})$ form and the concrete term carries the width $2 \cdot B \cdot f_{c,eff}$ consistent with bending about the strong axis; for the four-corner Zhao layout a parallel set of sub-cases applies. For the second cruciform scenario ($b^*/2 < h_n \le d_d/2$), which together with the first scenario covers the four eccentric Bogdan specimens, axial equilibrium between B and C gives the closed form

$$h_n = \frac{N_{pm,Rd} - 2A_{a,one}(2f_{y,eq} - f_{c,eff})}{2Bf_{c,eff} + 4b_{s2}(2f_s - f_{c,eff})} \quad (7)$$

with $W_{sn} = 2 \cdot b_{s2} \cdot h_n^2$ and $W_{cn} = B \cdot h_n^2 - W_{yn} - W_{sn}$, and $h_n \approx 20$–31 mm for these specimens. All polygon coordinates therefore follow from the plastic stress distribution without empirical multipliers.

4.3. Prediction of the failure load at a given eccentricity

For each specimen, the predicted failure

force at the actual eccentricity e is the intersection of the radial load line M = N·e with the polygon A → C → D → B. On segment A–C, where $M_A = 0$ and $M_C = M_{pl,Rd}$, this intersection has the closed form

$$N_{pred} = N_{pl,Rd} + t(N_{pm,Rd} - N_{pl,Rd})$$

$$t = \frac{eN_{pl,Rd}}{M_{pl,Rd} - e(N_{pm,Rd} - N_{pl,Rd})} \quad (8)$$

with e, N and M in consistent units. For all four eccentric specimens, the load line falls on this segment, since the eccentricity at point C ($e_C = M_{pl,Rd}/N_{pm,Rd} \approx 148$ mm for E10-1) exceeds the maximum tested eccentricity of 89.6 mm (E15-1), and the interpolation parameter t lies in the range 0.56–0.79; for the five axial specimens, the line degenerates to point A, so $N_{pred} = N_{pl,Rd}$. The procedure is fully closed-form and free of numerical iteration. Consistent with Section 2.1, the second-order effect is carried on the demand side through the measured eccentricities, and no member-stability provision of the three standards enters the prediction.

5. Comparison of code predictions with the experimental results

5.1. Predicted versus measured capacities

Table 4 reports, for each specimen, the measured peak force N_{test}, the moment $M_{test} = N_{test}·e$ at the critical section, and the axial force N_{pred} and moment M_{pred} predicted at the same eccentricity by the two distinct streams - the coincident EN 1994-1-1 and AISC 360-22 prediction, and the JGJ 138-2016 prediction; Table 5 gives the test-to-prediction ratios $\lambda = N_{test}/N_{pred}$ and their statistics. The polygonal surfaces are plotted in Fig. 4 and the ratios against eccentricity in Fig. 5. Two reading conventions hold throughout: the ratio λ is defined on the axial force at the common eccentricity, so that λ > 1 denotes a safe-sided prediction and λ < 1 a non-conservative one; and the moment columns of Table 4 give the predicted moments $M_{pred} = N_{pred}·e$ at that same eccentricity, non-zero for the four eccentric specimens only.

Table 5. Test-to-prediction ratios $\lambda = N_{test}/N_{pred}$ and summary statistics.

Specimen	Group	λ (EN 1994-1-1 = AISC 360-22)	λ (JGJ 138-2016)
E00-1	Axial	0.899	0.837
E00-2	Axial	0.878	0.815
E10-1	e/h ≈ 12%	1.120	1.031
E10-2	e/h ≈ 13%	1.048	0.977
E15-1	e/h ≈ 20%	1.137	1.047
E15-2	e/h ≈ 18%	1.159	1.071
A1	Axial	1.237	1.122
A2	Axial	1.261	1.128
A3	Axial	1.295	1.169
Mean (Bogdan, n = 6)		1.040	0.963
CoV (%)		11.9	11.5
Min / Max		0.878 / 1.159	0.815 / 1.071
Mean (Zhao, n = 3)		1.264	1.139
CoV (%)		2.3	2.3
Mean (all, n = 9)		1.115	1.022
CoV (%)		13.4	12.2
Min / Max		0.878 / 1.295	0.815 / 1.169

5.2. Discussion of the comparison

Fig. 4 shows a single representative polygon in each panel - E10-1 for the Bogdan group and A1 for the Zhao group–each built with its own

measured f'_c and f_y; the between-specimen variation of the vertices stays within about 6%, so the representative polygon is a faithful visual proxy, while the ratios of Tables 4 and 5 are computed individually against each specimen's own polygon.

In the Zhao panel, the EN 1994-1-1 and AISC 360-22 polygons coincide, while the JGJ 138-2016 polygon lies outside them; its $\alpha_1 = 1$ for $f_{ck} \leq 50$ MPa, leaving the full concrete stress in place. Three findings follow.

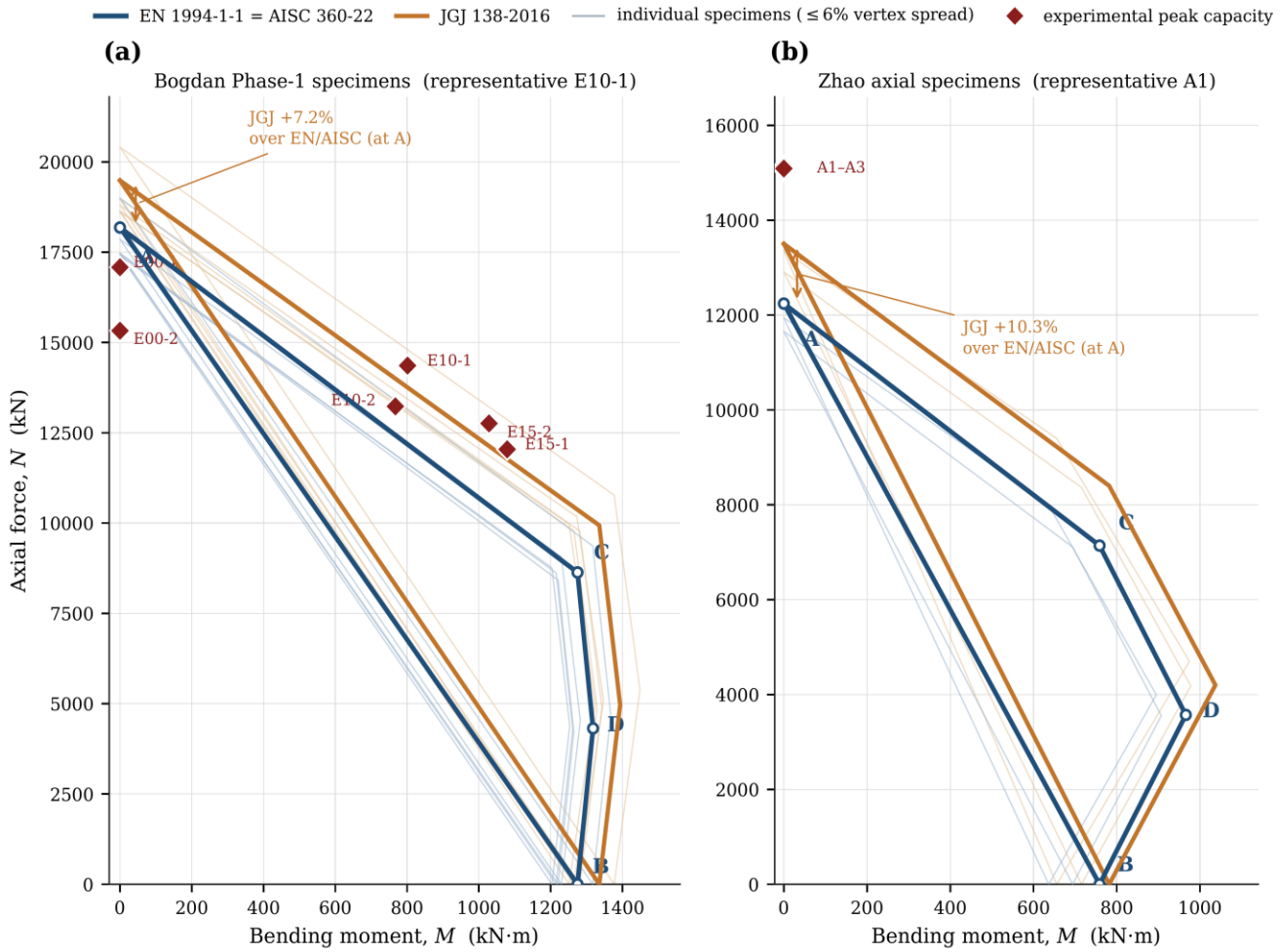


Fig. 4. Experimental peak capacities (markers) and predicted interaction polygons of the two streams (EN 1994-1-1 = AISC 360-22, and JGJ 138-2016): (a) Bogdan Phase-1 (representative E10-1); (b) Zhao axial (representative A1). Vertex variation between specimens ≤ 6%.

First, the predictions are generally conservative over the eccentric range and for the cage-type Zhao configuration (the single exception being E10-2 under JGJ 138-2016, λ = 0.977), but carry a localised non-conservative bias confined to the two pure-axial Bogdan specimens. The test-to-prediction ratios of the five axially loaded specimens span 0.88–1.30 for the coincident EN 1994-1-1 and AISC 360-22 prediction and 0.81–1.17 for JGJ 138-2016; E00-1 and E00-2 sit at the lower edge, with EN 1994-1-1 and AISC 360-22 overestimating the measured capacity by 11–14% (λ = 0.88–0.90) and the less conservative JGJ 138-2016 by 19–23% (λ = 0.81–0.84). Part of the bias has a material-input origin, quantified in Section 2.2; the remainder originates in the non-attainment of the full plastic axial state at peak, for two compounding reasons evidenced in the source tests. First, the strain measurements reported for the pure-axial specimens show the longitudinal bars and the encased profiles still elastic at the peak load, with failure initiated by the concrete in compression before the steel yield strains are reached [1,18], so the steel had not developed the

full yield force that the plastic-stress-distribution method assumes; because pure-axial loading mobilises the whole section at a single strain, the prediction is the most sensitive of all configurations to this shortfall. Second, the unconfined cover crushes before the code strain (ε_{cu1} = 3.5 × 10^{-3} in EN 1992-1-1, falling to about 3.0 × 10^{-3} at f_{ck} = 60 MPa) is reached across its depth, an effect that intensifies with cylinder strength into the 55–61 MPa range encountered here and that is compounded by an in-place strength below the companion value, which Bogdan et al. [1] attribute to the age, casting and curing of the member and which Lai et al. [8] and Wang et al. [9] document for high-strength encased sections; the uniform block is therefore not realised over the full area. The two mechanisms act in the same direction - neither the steel nor the concrete delivers its assumed plastic stress at the measured peak - which is why the bias concentrates in the pure-axial Bogdan specimens and, by contrast with the strain-hardened steel of the Zhao specimens (see the second finding below), does not spread across the database. A second, non-material contribution should also be recorded. Bogdan et al. [2] report peak moments of 143 and 52 kN·m for the two nominally concentric specimens, corresponding to eccentricity ratios of 1.9% and 0.8% arising from horizontal deflections recorded during the test. Evaluating the polygon at those residual eccentricities instead of at vertex A raises λ from 0.899 to 0.956 for E00-1 and from 0.878 to 0.901 for E00-2 under EN 1994-1-1 = AISC 360-22 (from 0.837 to 0.888 and from 0.815 to 0.835 under JGJ 138-2016). The pure-compression vertex is retained as the benchmark in Tables 4 and 5, since these specimens were loaded concentrically and the source regards the residual moments as too small to influence the axial resistances, but the two evaluations bracket the deviation reported here. For the four eccentric Bogdan specimens, the strain gradient leaves only part of the section at the critical strain at peak load, so the block is realised over a sufficient fraction of the area, and the capacities are recovered, generally conservatively, by 5–16% (λ = 1.048-1.159 for EN 1994-1-1 and AISC 360-22). The eccentric subset is at once more conservative and far less scattered (CoV ≈ 4.3% versus ≈ 18.6% for EN 1994-1-1 = AISC), because the strain gradient suppresses the single mechanism–full-area mobilisation of a reduced in-place strength–that destabilises the pure-axial predictions.

Second, the Zhao specimens are under-predicted by every code, tightly and almost uniformly - λ = 1.24–1.29 for the coincident EN 1994-1-1 and AISC 360-22 prediction and 1.12–1.17 for JGJ 138-2016, at an intra-source CoV of about 2.3%. The tightness points to a single systematic mechanism common to the three specimens rather than to specimen-to-specimen scatter, but that mechanism is not the confinement of the inner core. Zhao et al. [5] report that the peak is reached as the unconfined cover crushes while the steel-cage-confined core has barely expanded, so the confinement enhancement - whose factors k_{hscc} = f'_{cc}/f'_c reach 1.44–1.76 only at the much higher confined-concrete peak strain $\varepsilon_{cc} = \varepsilon_c[1 + 5(k - 1)]$ - is not mobilised at the load that governs λ; consistent with this, the measured peaks are nearly identical (15,143, 15,058 and 15,089 kN) across battens spanning k_{hscc} from 1.44 to 1.76, and the residual differences in λ track the steel grade (largest for A3 at f_y = 261 MPa) rather than k_{hscc} (largest for A1, yet smallest λ). The under-prediction is therefore dominated by the conservatism of the effective concrete block for these stocky, machine-loaded specimens, in which the concrete attains close to its full cylinder strength at peak: replacing the 0.85 block by the near-unity JGJ α_1 recovers roughly half of the margin (λ falls from 1.24–1.29 to 1.12–1.17), and the residual 12–17% implies a section response equivalent to a concrete stress of order $1.2 \cdot f'_c$, shared between the strain-hardening reserve of the low-grade steel (f_y = 261–300 MPa against f_u = 405–453 MPa), unused by the rigid-plastic

assumption, and an early triaxial gain in the concrete adjacent to the profiles. The confined core is thus best read as a post-peak ductility reserve, in the sense of Zhao et al. [5], rather than as a peak-capacity contribution that the simplified method discards. This reading is a trend consistent with, though not attributable solely to, the two configurations: the two campaigns also differ in member length and slenderness (L/h = 6.0 against 3.3), end conditions, steel ratio and yield strength, concrete strength and loading, so the present database does not permit the configuration effect to be isolated from these concurrent factors.

Third, EN 1994-1-1 and AISC 360-22 return identical predictions across the database, and it is JGJ 138-2016 that stands apart. Because JGJ carries $\alpha_1 \cdot f_{ck}$ rather than $0.85 \cdot f_{ck}$, and α_1 remains at unity for the three Zhao specimens ($f_{ck} \leq 50$ MPa) and falls no lower than about 0.95 across the Bogdan specimens, its effective concrete stress is the largest of the three; it therefore predicts the highest capacity and the lowest λ, by a margin of about 8% for the Bogdan specimens and 10–12% for the Zhao specimens over the coincident EN/AISC value. This makes JGJ the least conservative standard for this column type and it is the only one that dips below unity beyond the two pure-axial Bogdan specimens, marginally so at the eccentric E10-2 (λ_{JGJ} = 0.977). The same mechanism that produces the AISC–JGJ spread amplifies with the concrete fraction of N_{pl}, which rises from roughly half for the Bogdan specimens to about two-thirds for the Zhao specimens — the Zhao profiles combine a smaller area with a lower yield strength - so the JGJ margin over EN/AISC is largest for the Zhao subset; Section 6 shows the same dependence recurring as the cylinder strength increases. Across the full set the means of λ are 1.12 (EN 1994-1-1 = AISC 360-22) and 1.02 (JGJ 138-2016) with coefficients of variation of 13.4% and 12.2%; the dispersion is dominated by the contrast between the pure-axial Bogdan specimens (λ ≈ 0.81–0.90) and the cage-type Zhao specimens (λ ≈ 1.12–1.29) rather than by any code-specific scatter, and Fig. 5 confirms that every data point except the two pure-axial Bogdan points (and, for JGJ alone, E10-2) sits on or above the λ = 1 line.

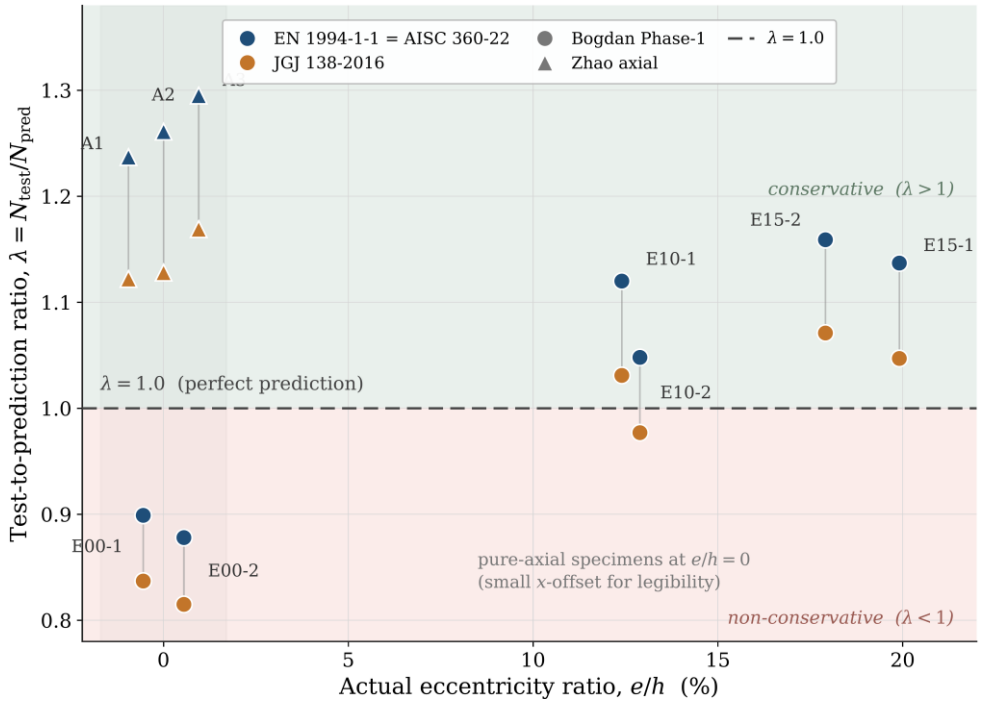


Fig. 5. Test-to-prediction ratio $\lambda = N_{test}/N_{pred}$ against the actual eccentricity ratio e/h for the two prediction streams (EN 1994-1-1 = AISC 360-22, and JGJ 138-2016); the dashed line at λ = 1.0 marks perfect prediction.

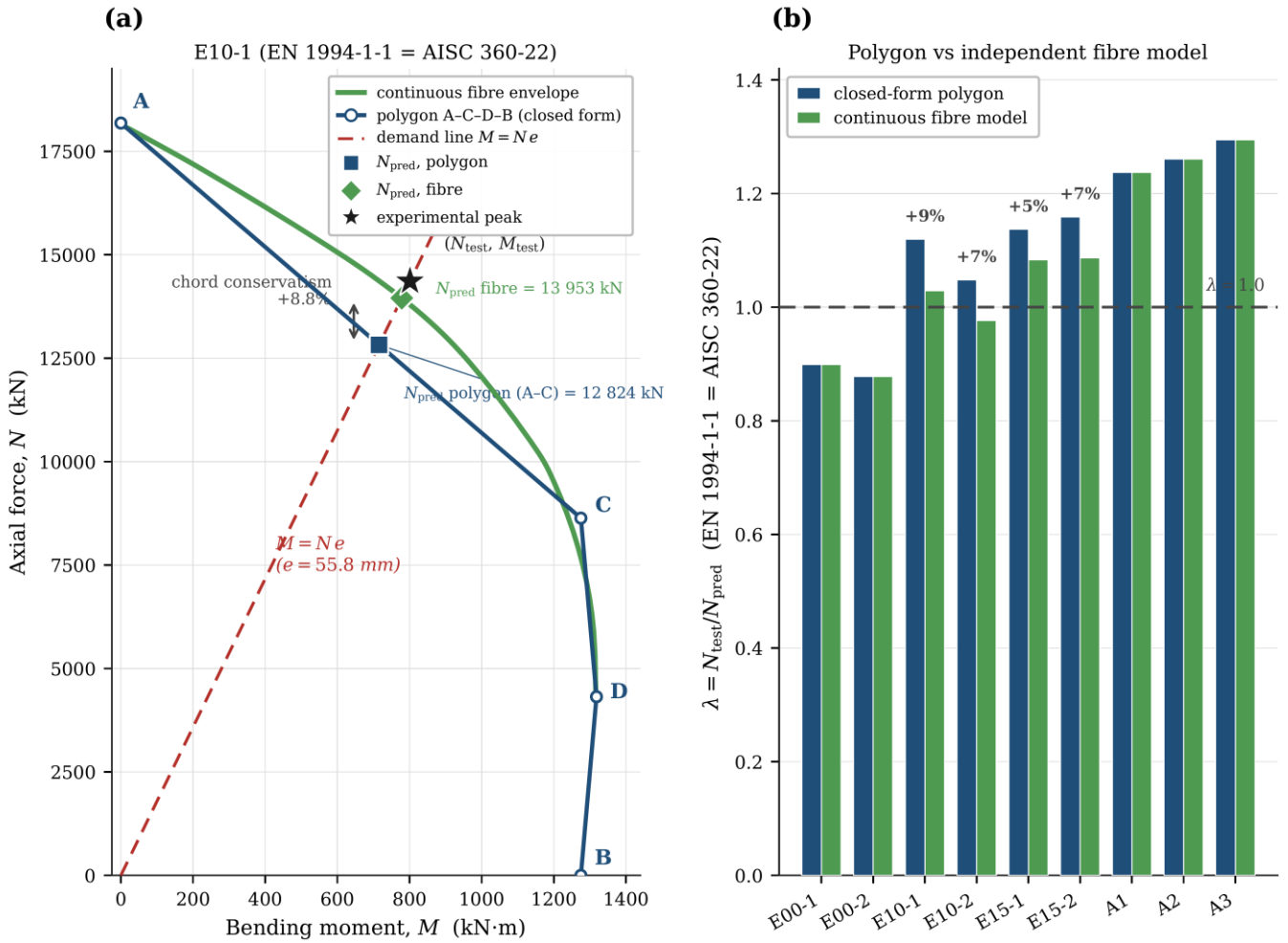


Fig. 6. Fibre-section verification of the four-point polygon (EN 1994-1-1 = AISC 360-22): (a) E10-1, fibre envelope versus inscribed polygon A–C–D–B, demand line M = N·e crossing ~8.8% above the A–C chord; (b) $\lambda = N_{test}/N_{pred}$ for the nine specimens, polygon versus fibre.

5.3. Independent fibre-section verification of the polygon construction

The four-point polygon is an inscribed chord approximation of the continuous plastic interaction surface, and its accuracy was checked against an independent fibre-section model built on the same constitutive idealisation - structural steel and reinforcement at $\pm f_y$, the concrete carrying the code uniform block $0.85 \cdot f_{ck}$ over the compressed depth and nothing in tension - but tracing the full N–M envelope by sweeping the plastic neutral axis through the discretised section rather than interpolating between four vertices. The model was first verified against the worked example of CTBUH [18]: it reproduces the axial capacity to within 0.07% (N_{pl} = 660,544 kN against 660,097 kN), the concrete-only force N_{pm} and the maximum moment M_{max} to within 0.4%, and recovers M_{max} at an axial force of $0.5 \cdot N_{pm}$ as the construction requires, so the fibre engine and the polygon rest on a common reference. For each of the nine specimens, the four polygon vertices fall on the fibre envelope, confirming the closed-form coordinates of Section 4.2.

The verification isolates the conservatism of the chord. For the five pure-axial specimens, the demand degenerates to vertex A, where the polygon and the fibre model return the same N_{pl} by construction, so the axial λ of Table 5 are exact, and the pure-axial bias identified in Section 5.2 is a property of the material input rather than of the polygon. For the four eccentric Bogdan specimens the radial demand line crosses the smooth fibre envelope (Fig. 6) at an axial capacity 5.0–8.8%

above the inscribed A–C chord (8.8% at E10-1, 5.0% at E15-1), because the chord lies inside the convex envelope between vertices A and C; the polygon is therefore conservative by construction under eccentric loading, and the eccentric λ for EN 1994-1-1 = AISC 360-22 in Table 5 (mean 1.12) carry a built-in chord margin of this order over the fibre prediction (mean fibre λ = 1.04). The check confirms the polygon implementation and bounds its discretisation error, but - sharing the plastic-block assumptions of the codes - it does not constitute an independent test of those assumptions against the measured response, which remains the role of the test-to-prediction ratios.

6. Sensitivity to the concrete cylinder strength

Table 6. Sensitivity of the predicted capacity at e/h = 12.5% to the concrete cylinder strength. The reduction factor α_1 is keyed to f_{ck} (column 1); the equivalent cube strength (column 2) is shown for reference only and does not enter the α_1 look-up.

f_{ck} (MPa)	Equivalent f_{cu} (MPa)	N_{EC4} = AISC (kN)	N_{JGJ} (kN)	N_{JGJ}/N_{EC4}
30	37.5	9,420	10,087	1.071
40	50.0	10,685	11,588	1.085
50	62.5	11,966	13,108	1.095
60	75.0	13,260	14,443	1.089
80	100.0	15,807	16,859	1.067
100	125.0	18,284	19,591	1.072
120	150.0	20,753	22,321	1.076
150	187.5	24,454	26,411	1.080
180	225.0	28,151	30,498	1.083

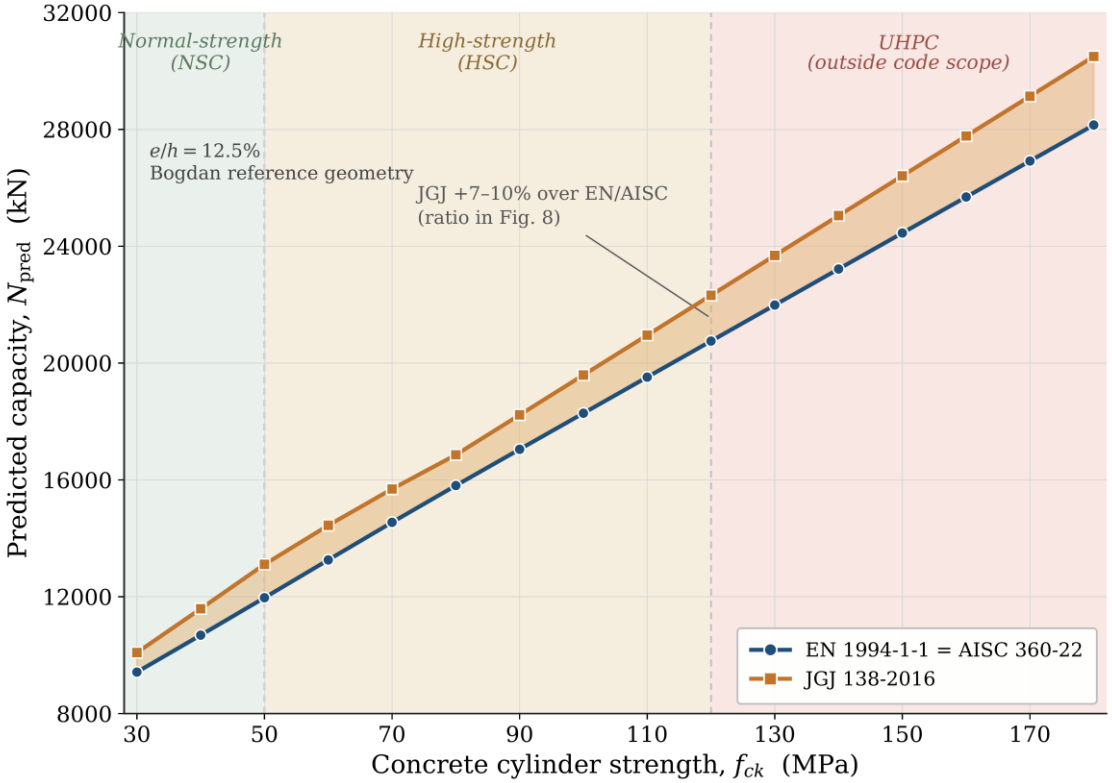


Fig. 7. Predicted capacity at e/h = 12.5% as a function of the concrete cylinder strength for the two prediction streams (EN 1994-1-1 = AISC 360-22, and JGJ 138-2016); the shaded bands mark the normal-strength, high-strength and UHPC ranges, the last lying outside the formal scope of all three standards.

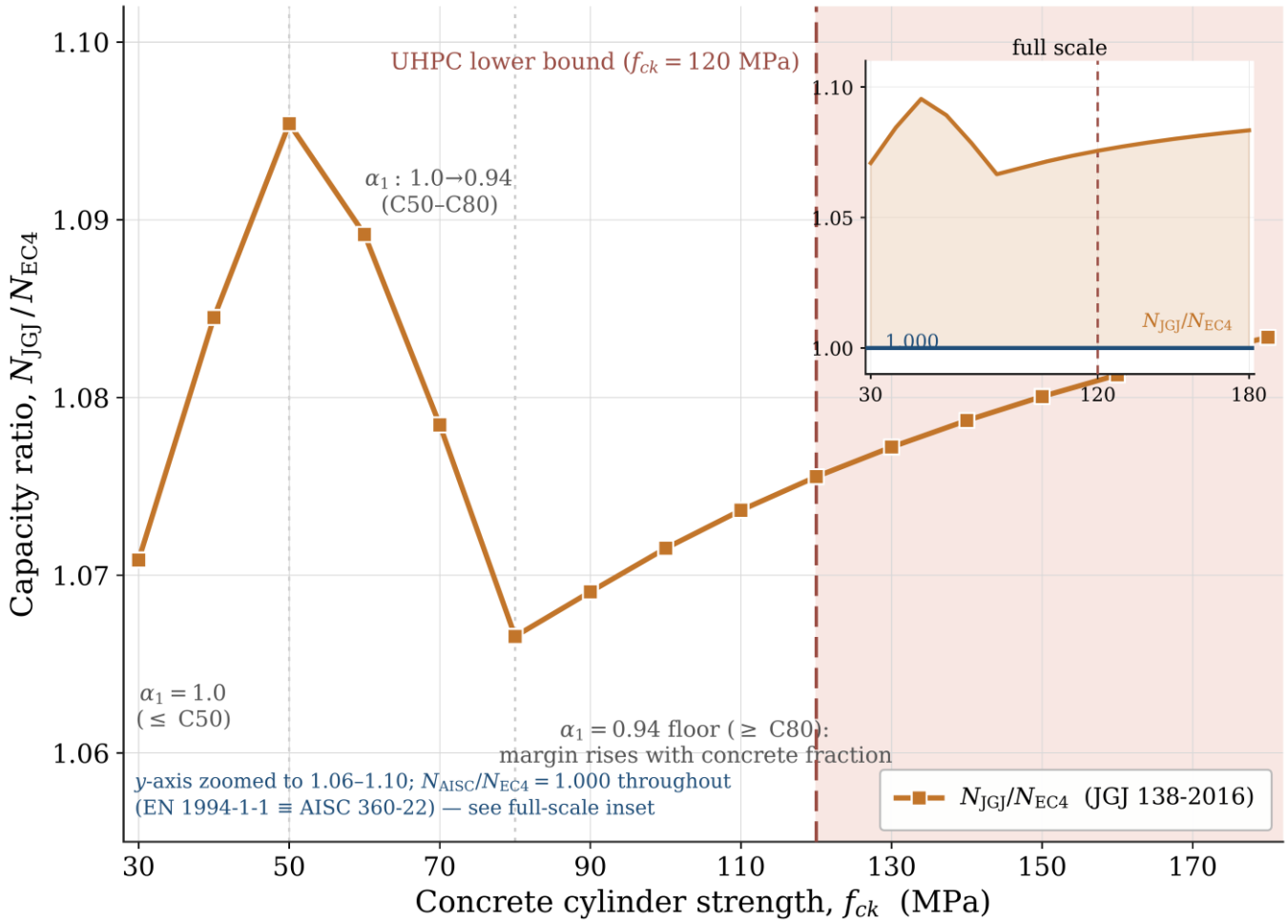


Fig. 8. Ratio N_{JGJ}/N_{EC4} against the concrete cylinder strength (N_{AISC}/N_{EC4} = 1.000 throughout, as EN 1994-1-1 and AISC 360-22 coincide); the vertical dashed line marks the lower bound of the UHPC range.

To examine the implications of applying the three codes to mega-columns of higher concrete strength than those tested, a parametric study was conducted. The cross-section geometry was that of Section 4.1 for the Bogdan specimens (d_p = 137.5 mm, A_a = 20,800 mm^2, A_s = 1,608.5 mm^2, cover 10 mm) and the steel-section and reinforcement yield strengths were fixed at $f_{y,eq}$ = 425 MPa and 438 MPa, representative of E10-1; the cylinder strength f_{ck} was varied over 30, 40, 50, 60, 80, 100, 120, 150 and 180 MPa, and the eccentricity ratio was held at e/h = 12.5% to remain within the validated range while avoiding pure-axial loading. Table 6 reports the predicted capacity and the ratio N_{JGJ}/N_{EC4} that quantifies the inter-code dispersion, with the EN 1994-1-1 and AISC 360-22 predictions being identical at every strength because both apply the 0.85 block; Figs. 7 and 8 plot the absolute capacities and the ratio.

The sweep retains each code's own effective stress block and the cross-sectional configuration and steel properties of the reference specimen unchanged. Its purpose is to map how the code formulas extrapolate when only the input strength varies, not to model UHPC behaviour. The features that distinguish UHPC lie outside the uniform-block idealisation, namely the fibre bridging of splitting cracks, the post-cracking tensile response, the altered cover-spalling behaviour and the interaction with confinement, and the evidence discussed in Section 7.3 [16, 22] indicates that without fibres the block overestimates capacity in this range. The eccentricity ratio is fixed at e/h = 12.5% because it lies inside the range over which the plane-section assumption was verified experimentally (e/h ≤ 15% [1]) while avoiding the

pure-axial condition, for which Section 5.2 identifies a material-level bias. The actual eccentricities of specimens E15-1 and E15-2, about 18–20% at peak load, exceeded the nominal 15% only through second-order growth and mark the limit of the validated range rather than its interior.

Two trends emerge. The ratio N_{AISC}/N_{EC4} is exactly unity at every strength, so the two standards extrapolate as one curve. The ratio N_{JGJ}/N_{EC4} stays above unity throughout—JGJ carries $\alpha_1 \cdot f_{ck}$ rather than $0.85 \cdot f_{ck}$ - and traces a shallow arc: it rises from 1.071 at f_{ck} = 30 MPa to a peak of 1.095 at the strength where α_1 first leaves unity - f_{ck} = 50 MPa on the cylinder-grade convention adopted here, or about 40 MPa were α_1 keyed to an equivalent cube grade—then relaxes to 1.067–1.089 as α_1 engages and trims the JGJ block, so that the JGJ generosity over the coincident EN/AISC prediction stays within the narrow band of 7–10% over the entire range under either convention. All three predictions grow monotonically and almost linearly with f_{ck}, without thresholds, so the simplified method extrapolates smoothly even when carried beyond its nominal scope. The interpolation parameter along segment A–C, however, migrates from 0.49 at f_{ck} = 30 MPa towards 0.94 at f_{ck} = 180 MPa as the rising concrete-only force N_{pm} draws point C down towards the demand line; the radial load line at e/h = 12.5% therefore remains on segment A–C throughout but approaches vertex C at the upper end of the range. The comparison between codes is a like-for-like one throughout, and the JGJ margin is a property of the concrete treatments rather than of a change in governing branch.

For the prospective use of UHPC, the more telling implication is qualitative rather than the magnitude of the dispersion: EN 1994-1-1 and AISC 360-22 both embed the 0.85 reduction of the effective concrete contribution, whereas JGJ 138-2016 reduces it only weakly through α_1, which bottoms out at 0.94. None of the three codes admits UHPC strength classes within its simplified method, and the 0.85 block itself is calibrated for normal- and high-strength rather than ultra-high-strength concrete (Section 7.3). The present results bound the problem usefully: because the inter-code dispersion reaches at most about 10% even at f_{ck} = 180 MPa whereas the pure-axial bias already reaches 11–14% for EN 1994-1-1 and AISC 360-22, and 19–23% for JGJ, at only 55–61 MPa, calibrating the effective concrete stress in the high-strength regime is a more pressing need than reconciling the codes with one another.

The results of Table 6 and Figs. 7–8 are extrapolations of the code mechanics beyond the formal scope of all three standards: beyond C50/60 for the simplified method of EN 1994-1-1:2004, beyond about 70 MPa for AISC 360-22 and beyond about C80 for JGJ 138-2016, the α_1 floor of 0.94 being itself an extrapolation above C80. They should not be read as predictions of UHPC member capacity; their role is confined to bounding the inter-code dispersion that a future calibration would have to resolve. Two internal drifts should be kept in view when the construction is pushed to this range. The interpolation parameter along segment A–C migrates from 0.49 at f_{ck} = 30 MPa towards 0.94 at f_{ck} = 180 MPa, and the governing sub-case of the plastic neutral axis migrates with it, from the first cruciform scenario at $f_{ck} \leq 60$ MPa, which is the range covering the tested specimens, to the second at 70–80 MPa and the third at $f_{ck} \geq 90$ MPa. The upper part of the sweep is therefore governed by a branch of the closed-form construction that the nine-specimen benchmark does not exercise.

7. Discussion and design implications

7.1. Adequacy of code superposition for the multi-profile cross-section

The comparison of Section 5 shows that the superposition principle common to all three codes reproduces the capacities in a generally conservative manner, with an accuracy comparable to that reported for single-profile encased columns of normal-strength concrete in

earlier validation exercises [23, 24, 25], for which test-to-prediction means of the order of 1.05–1.15 and coefficients of variation of 10–15% are typical, and the scatter here is dominated by between-source differences, which cannot be attributed solely to the cross-sectional configuration (Section 5.2), rather than by any code-specific term. The practical implication is that, with the confinement and cover detailing of either campaign, the simplified capacity may be computed by treating the four profiles as a single equivalent steel area at their actual centroid positions, without a dedicated multi-profile correction—a conclusion that extends the shear-focused finding of Plumier et al. [3] to axial-flexural interaction across two independent programmes.

7.2. Equivalence of EN 1994-1-1 and AISC 360-22, and the lesser conservatism of JGJ 138-2016

EN 1994-1-1 and AISC 360-22 return identical simplified predictions for this column type, because both apply the 0.85 effective-stress block to the encased concrete (Section 3.1). The equivalence is a property of the cross-sectional plastic resistance alone. When the same six specimens are assessed at member level, with each standard's own stability reduction and additional eccentricities, CTBUH [18] obtains mean test-to-prediction ratios of 1.17 for EN 1994-1-1 against 1.51 for AISC-LRFD, so the two standards diverge substantially once the member provisions are engaged. The distinguishable margin is therefore JGJ 138-2016, which returns capacities 7–12% above the coincident EN/AISC value across the nine test specimens (about 8% for the Bogdan subset and 10–12% for the Zhao subset), and 7–10% in the parametric sweep at e/h = 12.5% (Section 6), because its α_1 factor stays at or near unity over the tested range while the other two carry the full 0.85 reduction. At the characteristic level considered here, EN 1994-1-1 and AISC 360-22 give the more conservative simplified prediction for this column type, and JGJ 138-2016 the least conservative. Whether that ordering persists at the design level depends on each standard's partial-factor and resistance-factor format (γ_c, γ_s and γ_a in EN 1994-1-1; ϕ_c in AISC 360-22; the design strengths and γ_{RE} in JGJ 138-2016), which this study does not examine. Retaining the factor 0.9 that JGJ 138-2016 places ahead of its stability coefficient (see Section 3.3 above) would lower the JGJ predictions by 10% and reverse the ordering, JGJ becoming 2–3% more conservative than the coincident EN/AISC value. A practitioner applying that code in full therefore obtains a capacity marginally below the EN/AISC value, and the ordering reported here should be read as a property of the cross-sectional mechanics rather than as a statement about design outcomes. Designers seeking the economic benefit of high-strength concrete up to about C80 may prefer the JGJ route, subject to the understanding that its calibration was developed below this strength and that its reduced margin should be matched by stricter detailing when extrapolating upward.

7.3. Implications for the application of UHPC

Two points from Section 6 carry into the prospective use of UHPC. The absolute spread of code predictions stays narrow, so the choice of code is not the dominant uncertainty in a UHPC mega-column design. The dominant uncertainty is the absence of any code-validated effective concrete block for UHPC: the tests of Lai et al. [16] on C130/S690 encased stub columns and of Chang et al. [25] on fibre- and stirrup-confined UHPC together indicate that, with about 2% of steel fibres and closely spaced stirrups, the superposition principle remains acceptable, whereas without fibres the codes overestimate the capacity. Mechanically, the fibres bridge the splitting cracks that precipitate cover spalling and sustain a residual tensile stress across them, so that the unconfined cover keeps carrying load up to the strain at which the code uniform block is mobilised; this is the same mechanism whose absence produces the pure-axial bias of Section

5.2. Any future extension to UHPC mega-columns should therefore provide a calibrated effective concrete stress—plausibly a reduction below the 0.85 block shared by EN 1994-1-1 and AISC 360-22, or a deeper engagement of the JGJ α_1 factor, at $f'_c \geq 100$ MPa—impose a minimum steel-fibre dosage to suppress cover spalling, and verify the eccentricity range over which the plane-section assumption holds ($e/h \leq 15\%$, after Bogdan et al. [1]).

7.4. Limitations

Several caveats define the scope. The benchmark comprises only nine monotonic specimens from two campaigns sharing a 450 × 450 mm section with four encased profiles (in a cruciform arrangement for the Bogdan specimens and at the four corners for the Zhao specimens), structural-steel ratios of 5.4–10.3%, profile yield strengths of 261–429 MPa, concrete strengths of 44.8–61.2 MPa and eccentricity ratios up to about 20% at peak load; broader conclusions need companion campaigns (e.g. Wang et al. [26], the high-performance-material study of Bogdan et al. [27]) and other dimensions and arrangements. The cyclic Phase-2 specimens of Bogdan et al. [1] meet the JGJ 3-2010 [28] drift requirements, but the polygonal approach does not cover cyclic capacity. The four-point polygon is itself a simplification; its eccentric conservatism is quantified at 5–9% by the fibre-section model of Section 5.3, whereas finite-element analyses would yield smooth surfaces [23, 29]. The sensitivity study of Section 6 is purely numerical and shows only how the formulas extrapolate, not experimental evidence in the UHPC range. Re-evaluating the predictions under two alternative concrete-strength conventions—$f'_c = f_{c,axial}/0.85$, which removes the 0.85 block, and $f'_c = 0.80 \cdot f_{cu}$, the cube-based route—leaves the qualitative conclusions intact (JGJ the least conservative, the architecture-driven scatter, the safe-sided eccentric range), yet moves the mean Bogdan EN/AISC ratio from 1.04 on the adopted $f_{c,axial}$ basis to 1.05 and 1.21 respectively; the pure-axial bias in fact deepens under the first convention, since removing the 0.85 block raises the predicted axial capacity. The $f_{c,axial}$ basis is adopted because it is the directly measured uniaxial strength, requiring no conversion factor. Finally, slenderness, second-order P–δ amplification and creep, increasingly important at UHPC strengths, are left for a follow-up study, and the Zhao battens are idealised as non-structural, consistent with the codes' neglect of confinement; modelling their restraint would raise the predicted Zhao capacities (see the second finding of Section 5.2 and the Conclusions, Section 8).

8. Conclusions

This study assessed how accurately EN 1994-1-1, AISC 360-22 and JGJ 138-2016 predict the capacity of mega-columns containing several encased hot-rolled profiles when their simplified provisions are extended by superposition, using one closed-form plastic-stress-distribution engine applied identically to a nine-specimen benchmark. The main conclusions are the following. These conclusions apply within the parameter range of the benchmark database: 450 × 450 mm square sections with four hot-rolled encased profiles in a cruciform (Bogdan) or four-corner (Zhao) arrangement, structural-steel ratios of 5.4–10.3%, profile yield strengths of 261–429 MPa, concrete strengths of 44.8–61.2 MPa, and eccentricity ratios up to about 20% at peak load. Their extension to other dimensions, profile types and arrangements, or strength grades requires further experimental evidence.

Within the unified cross-sectional framework adopted here, the plastic stress distribution at the characteristic material level, EN 1994-1-1 and AISC 360-22 give identical predictions for fully encased members, since both apply the 0.85 effective-stress block; this equivalence is limited to the formulation adopted in the present study and does not extend to the complete design procedures, whose stability provisions and safety formats differ. Both recover the measured

capacities in a generally conservative manner over the eccentric range and for the cage-type configuration, with the scatter governed by differences between test sources rather than by any code-specific term; across the database, the mean test-to-prediction ratios are 1.12 (EN 1994-1-1 = AISC 360-22) and 1.02 (JGJ 138-2016), at coefficients of variation of 13.4% and 12.2%.

JGJ 138-2016 is the least conservative of the three (about 7–12% above the coincident EN 1994-1-1 = AISC 360-22 value across the nine specimens, and 7–10% in the parametric sweep at e/h = 12.5%), and the only standard that turns non-conservative beyond the pure-axial specimens.

A localised non-conservative bias affects the two pure-axial specimens in the high-strength regime, more severely for JGJ, by 19–23% against 11–14% for EN 1994-1-1 = AISC 360-22. It stems from the full plastic state not being reached at peak—the steel still at or below yield and the high-strength cover spalling prematurely—rather than from any single material shortfall (Section 5.2). Because the bias is independent of the number of profiles, the superposition principle remains defensible at the cross-section level.

The contrast between the Bogdan and Zhao specimens is consistent with two architectural sub-classes, a discrete-profile section that develops composite action through the surrounding concrete and a battened-cage section that confines an inner core. The two campaigns also differ in member lengths, end conditions, material strengths, and loading conditions; therefore, the configuration effect cannot be isolated using the present database, and the observation is reported only as a trend. Since Zhao et al. [5] show that the confined core is not mobilised at the peak that governs the capacity, the under-prediction of the cage-type specimens is read as conservatism of the effective concrete block for these stocky specimens, with the confined core acting as a post-peak ductility reserve. Future calibration on a database that varies the configuration at otherwise matched parameters is recommended.

As the cylinder strength is swept towards the UHPC range, EN 1994-1-1 and AISC 360-22 remain identical, and the only inter-code dispersion is the JGJ margin, which holds within a narrow band of about 7–10% up to 180 MPa in the parametric sweep at e/h = 12.5% rather than widening, and none of the standards formally admits UHPC within its simplified method.

Overall, the design problem separates into a secondary source of uncertainty—the choice of code—and the primary ones—the cross-sectional architecture and the effective concrete stress in the high-strength, pure-axial regime. The recommended next steps are a finite-element parametric study with a UHPC-calibrated concrete damage-plasticity model checked against the present predictions, a broader experimental base, and a reliability-based recalibration of resistance factors that distinguishes discrete-profile from cage-type configurations. The conclusions above refer to characteristic-level resistances computed with partial safety factors set to unity. They do not extend to factored design capacities, which also reflect the different safety formats of the three standards.

Acknowledgments

This work was carried out within the 2026–2027 research programme of the Vietnam Aviation Academy.

Declaration of Generative AI

During the preparation of this work, the authors used Claude (Anthropic) in order to check the calculations and to improve the language of the manuscript. After using this tool, the authors reviewed and edited the content as needed and take full responsibility for the content of the published article.

References

[1]. T. Bogdan, J.-C. Gerardy, D.W. Davies, N. Popa. (2017). 08.07: Performance and capacity of composite “mega columns” with encased hot rolled steel sections. *ce/papers*, 1(2-3), 1879-

1888. https://doi.org/10.1002/cepa.232

[2]. T. Bogdan, M. Chrzanowski, C. Odenbreit. (2019). Mega columns with several reinforced steel profiles – Experimental and numerical investigations. *Structures*, 21, 3-21. https://doi.org/10.1016/j.istruc.2019.06.024

[3]. A. Plumier, T. Bogdan, H. Degée. (2012). Design of column with several encased steel profiles for combined compression and bending. *Internal Report, University of Liège – ArcelorMittal, Liège, Belgium.*

[4]. CEN. (2004). EN 1994-1-1:2004 – Eurocode 4: Design of composite steel and concrete structures – Part 1-1: General rules and rules for buildings. *European Committee for Standardization.*

[5]. X. Zhao, F. Wen, S. Yan. (2022). Behavior of multi-steel reinforced concrete columns with encased steel H-sections. *Engineering Structures*, 264, 114463. https://doi.org/10.1016/j.engstruct.2022.114463

[6]. AISC. (2022). ANSI/AISC 360-22 – Specification for Structural Steel Buildings. *American Institute of Steel Construction*.

[7]. MOHURD. (2016). JGJ 138-2016 – Code for design of composite structures. Ministry of Housing and Urban-Rural Development, Beijing (in Chinese).

[8]. B. Lai, J.Y.R. Liew, M. Xiong. (2019). Experimental study on high strength concrete encased steel composite short columns. *Construction and Building Materials*, 228, 116640. https://doi.org/10.1016/j.conbuildmat.2019.08.021

[9]. J. Wang, Y. Duan, Y. Wang, X. Wang, Q. Liu. (2021). Analysis and Modification of Methods for Calculating Axial Load Capacity of High-Strength Steel-Reinforced Concrete Composite Columns. *Materials*, 14(22), 6860. https://doi.org/10.3390/ma14226860

[10]. R. Yu, P. Spiesz, H.J.H. Brouwers. (2015). Development of an eco-friendly Ultra-High Performance Concrete (UHPC) with efficient cement and mineral admixtures uses. *Cement and Concrete Composites*, 55, 383-394. https://doi.org/10.1016/j.cemconcomp.2014.09.024

[11]. B.A. Graybeal. (2006). material property characterization of ultra-high performance concrete. Report No. FHWA-HRT-06-103. Federal Highway Administration.

[12]. J. Wei, Z. Xie, W. Zhang, X. Luo, Y. Yang, B. Chen. (2021). Experimental study on circular steel tube-confined reinforced UHPC columns under axial loading. *Engineering Structures*, 230, 111599. https://doi.org/10.1016/j.engstruct.2020.111599

[13]. Q.X. Wu, Z.K. Xu, H.H. Yuan, Z.Q. Qin. (2026). Structural performance study on UHPC-encased CFST composite stub columns under eccentric compression. *Engineering Mechanics*, 43(3), 233-248. (in Chinese) https://doi.org/10.6052/j.issn.1000-4750.2023.08.0622

[14]. H. Tang, J. Qin, Y. Liu, J. Chen. (2023). Axial compression behaviour of circular and square UHPC-filled stainless steel tube columns. *Journal of Constructional Steel Research*, 211, 108111. https://doi.org/10.1016/j.jcsr.2023.108111

[15]. X.-Y. Min, L. Tan, D.-F. Li, Y.-L. Chen, J.-L. Chai, J.-Z. Tong. (2025). Numerical analysis and resistance design of UHPC- and UHTCC-encased rectangular steel tubular columns subject to axial compression. *Buildings*, 15(20), 3735. https://doi.org/10.3390/buildings15203735

[16]. B. Lai, J.Y.R. Liew, A.L. Hoang. (2019). Behavior of high strength concrete encased steel composite stub columns with C130 concrete and S690 steel. *Engineering Structures*, 200, 109743. https://doi.org/10.1016/j.engstruct.2019.10974

3

[17]. K. Megahed. (2025). Strength prediction of ECC-CES columns under eccentric compression using adaptive sampling and ML techniques. *Scientific Reports*, 15, 1202. https://doi.org/10.1038/s41598-024-83666-z

[18]. F. Deng, T. Chen, C. Xiao. (2016). Performance and capacity of isolated steel reinforced concrete columns and design approaches. *Research report, China Academy of Building Research (CABR) Technology Co., Ltd., Beijing, prepared for ArcelorMittal and coordinated by the Council on Tall Buildings and Urban Habitat.*

[19]. MOHURD and SAMR. (2019). GB/T 50081-2019 – Standard for test methods of concrete physical and mechanical properties. China Architecture & Building Press (in Chinese).

[20]. CEN. (2026). EN 1994-1-1:2026 – Eurocode 4: Design of composite steel and concrete structures – Part 1-1: General rules and rules for buildings. *European Committee for Standardization.*

[21]. MOHURD. (2010). GB 50010-2010 – Code for design of concrete structures (2015 edition). Beijing (in Chinese).

[22]. Y. Chang, J. Shi, Y. Hou, T. Lu. (2021). Experimental study on the uniaxial compression performance of ultrahigh-performance concrete constrained by stirrups and fibers. *Engineering Structures*, 243, 112656. https://doi.org/10.1016/j.engstruct.2021.112656

[23]. A. Behnam, M.D. Denavit. (2020). Plastic stress distribution method for predicting interaction strength of steel-concrete composite cross sections. *Journal of Constructional Steel Research*, 170, 106092. https://doi.org/10.1016/j.jcsr.2020.106092

[24]. M.D. Denavit, J.F. Hajjar, T. Perea, R.T. Leon. (2016). Stability analysis and design of composite structures. *Journal of Structural Engineering*, 142(3), 04015157. https://doi.org/10.1061/(ASCE)ST.1943-541X.0001434

[25]. B. Lai, J.Y.R. Liew, A. Venkateshwaran, S. Li, M. Xiong. (2020). Assessment of high-strength concrete encased steel composite columns subject to axial compression. *Journal of Constructional Steel Research*, 164, 105765. https://doi.org/10.1016/j.jcsr.2019.105765

[26]. J. Wang, X. Wang, Y. Duan, Y. Su, X. Yi. (2022). The investigation on mechanical performances of high-strength steel reinforced concrete composite short columns under axial load. *Materials*, 15(1), 329. https://doi.org/10.3390/ma15010329

[27]. T. Bogdan, O. Ergun, P. Schurgacz, O.M. Anwaar, M. Rich, M. Schäfer, M. Knobloch, W. Kurz. (2023). Load bearing behavior of concrete encased composite columns with high-performance materials. ce/*papers*, 6(3-4), 314-319. https://doi.org/10.1002/cepa.2705

[28]. MOHURD. (2010). JGJ 3-2010 – Technical specification for concrete structures of tall buildings (in Chinese).

[29]. B. Lai, J.Y.R. Liew. (2020). Axial-moment interaction of high strength concrete encased steel composite columns: Design recommendation. *Journal of Constructional Steel Research*, 170, 106136. https://doi.org/10.1016/j.jcsr.2020.106136